

The Bayesian Asteroseismology data Modeling pipeline and its application to *K2* data

JOEL C. ZINN,¹ DENNIS STELLO,^{1,2,3,4} DANIEL HUBER,^{5,2,3,6} AND SANJIB SHARMA^{2,4}

¹*School of Physics, University of New South Wales, Barker Street, Sydney, NSW 2052, Australia*

²*Sydney Institute for Astronomy (SIfA), School of Physics, University of Sydney, NSW 2006, Australia*

³*Stellar Astrophysics Centre, Department of Physics and Astronomy, Aarhus University, Ny Munkegade 120, DK-8000 Aarhus C, Denmark*

⁴*ARC Centre of Excellence for All Sky Astrophysics in 3 Dimensions (ASTRO 3D)*

⁵*Institute for Astronomy, University of Hawai'i, 2680 Woodlawn Drive, Honolulu, HI 96822, USA*

⁶*SETI Institute, 189 Bernardo Avenue, Mountain View, CA 94043, USA*

ABSTRACT

We present the Bayesian Asteroseismology data Modeling (BAM) pipeline, an automated asteroseismology pipeline that returns global oscillation parameters and granulation parameters from the analysis of photometric time-series. BAM also determines if a star is likely to be a solar-like oscillator. We have designed BAM to specially process *K2* light curves, which suffer from unique noise signatures that can confuse asteroseismic analysis, though it may be used on any photometric time series — including those from *Kepler* and TESS. We demonstrate the BAM oscillation parameters are consistent within $\sim 1.53\%$ (random) $\pm 0.2\%$ (systematic) and 1.51% (random) $\pm 0.6\%$ (systematic) for ν_{\max} and $\Delta\nu$ with benchmark results for typical *K2* red giant stars in the *K2* Galactic Archaeology Program's (GAP) Campaign 1 sample. Application of BAM to 13016 *K2* Campaign 1 targets not in the GAP sample yields 104 red giant solar-like oscillators. Based on the number of serendipitous giants we find, we estimate an upper limit on the average purity in dwarf selection among C1 proposals is $\approx 99\%$, which could be lower when considering incompleteness in BAM detection efficiency, and proper motion cuts specific to C1 Guest Observer proposals.

Keywords: asteroseismology, methods: data analysis, stars: oscillations

1. INTRODUCTION

Solar-like oscillators are stars that support standing acoustic waves excited by surface convection, and whose global frequency characteristics are determined by the stellar density and surface gravity (e.g., Ulrich 1986; Brown et al. 1991; Kjeldsen & Bedding 1995). The frequencies may be measured in radial velocity variations or in photometric variability. Detecting mode frequencies in solar-like oscillators yields precise determinations of fundamental stellar parameters like mass and radius. However, only about a dozen stars had been observed to exhibit solar-like oscillations prior to the results from the space-based CoRoT (Baglin et al. 2006) and *Kepler* (Borucki et al. 2008) missions. With improved photometric precision compared to ground-based observations, and continuous monitoring of many stars simulta-

neously for up to four years with *Kepler*, solar-like oscillations have been photometrically detected in thousands of stars — mostly red giants (e.g., De Ridder et al. 2009; Hekker et al. 2009; Bedding et al. 2010; Mosser et al. 2010; Stello et al. 2013; Yu et al. 2018). In light of these large asteroseismic data sets, several pipelines have been developed in order to automatically extract asteroseismic parameters (e.g., OCT [Hekker et al. 2010], CAN [Kallinger et al. 2010, 2014, 2016], COR [Mosser & Apourchaux 2009], A2Z [Mathur et al. 2010]).

Among these pipelines is SYD (Huber et al. 2009), much of whose success can be attributed to taking advantage of known scaling relations among stellar granulation, the frequency of maximum power (ν_{\max}), and the overtone frequency separation ($\Delta\nu$) (Kjeldsen & Bedding 2011) to provide accurate initial guesses for fitting parameters. A significant shortcoming of SYD (and other similar pipelines) is that it does not assess if a given star shows excess power from oscillations in a statistically robust way, hence requiring post-processing

and often visual verification. This introduces significant unknown, and subjective, detection bias, which hampers population analyses of the seismic sample. Ensuring reproducible selection functions is particularly important for applications aimed to perform Galactic archaeology studies [Stello et al. \(2017\)](#).

In this paper we introduce a new pipeline, the Bayesian Asteroseismology data Modelling Pipeline (BAM), which builds on the SYD pipeline with an eye toward automatic, robust classification of light curves. BAM formalizes relations among granulation, ν_{\max} , and $\Delta\nu$ through a Bayesian framework in which these relations are implemented as priors. It is this Bayesian framework that then allows for a self-consistent, statistical separation of oscillators from non-oscillators.

BAM was also developed with the particular challenges involved in extracting asteroseismic parameters from the re-purposed *Kepler* mission, *K2*, in mind. Following the failure of two of its reaction wheels, the *Kepler* satellite was re-aligned to point in the ecliptic plane. As opposed to *Kepler*'s single field of view in Cygnus, the *K2* pointing pattern covers the ecliptic plane with a footprint of about 100 square degrees, which is repositioned every ~ 80 days by typically ~ 90 degrees along the ecliptic. However, periodic small-angle pointing corrections are performed every six hours by firing the spacecraft thrusters, which introduce instrumental signatures in *K2* light curves. These features unfortunately correspond to typical frequencies of red giant oscillations, and can mimic true asteroseismic oscillations near $\sim 47\mu\text{Hz}$ (the 6 hour thruster firing frequency period). Because this instrumental feature overlaps in frequency with where a typical red clump star shows maximum oscillation power, it can hinder recovering red clump stars, which comprise the largest population of red giants in the Galaxy. BAM's Bayesian framework uses information like the amplitude of the power excess and the shape of the rest of the power spectrum to distinguish between *K2* thruster firing noise and genuine oscillations. In addition to this instrumental feature, the *K2* white noise level is typically larger than the white noise of the original *Kepler* mission by a factor of about two, depending on how the data are processed. (However, several *K2* light curve processing pipelines have reported near-*Kepler* white noise levels [[Vanderburg & Johnson 2014](#); [Lund et al. 2015](#); [Armstrong et al. 2015](#); [Aigrain et al. 2016](#); [Luger et al. 2016](#)].)

In addition to describing how BAM works in this paper, we apply it to extract global oscillation parameters for red giants observed serendipitously by *K2* through Guest Observer (GO) programs targeting dwarf stars during Campaign 1. This new sample of giants there-

fore adds to the already known red giant sample from [Stello et al. \(2017\)](#).

2. DATA

In this paper, we work with two sets of *K2* light curves: 1) the Campaign 1 (C1) target sample from the *K2* Galactic Archaeology Program (GAP; [Stello et al. 2015, 2017](#))¹, which comprises 8630 stars, and 2) all non-GAP C1 targets, of 13016 in total.² Results from BAM for the former sample have been published in [Stello et al. \(2017\)](#). We review some of those results here, and extend the application of BAM to the latter sample in order to identify serendipitous red giants.

All our C1 light curves have been generated by [Vanderburg & Johnson \(2014\)](#) (VJ), who perform aperture photometry on *K2* images and remove trends associated with centroid errors caused by the spacecraft's unstable pointing. We will show below that this preprocessing does not completely remove the thruster-induced instrumental features from the data, and therefore requires additional processing in BAM.

We begin by first removing trends on time-scales much longer than solar-like oscillation time-scales for the stars we are interested in. For each light curve, we perform high-pass filtering by dividing the VJ light curve by a 4-day wide boxcar-smoothed version of the light curve, thus imposing a high-pass cutoff frequency of $\sim 3\mu\text{Hz}$; frequencies below this limit are not considered in any of our analysis.³ Next, we fill in small gaps in the light curve of up to three consecutive points with linear interpolation, and remove 4σ outliers. This procedure results in a smoother power spectrum and less contamination from the spectral window, without biasing global oscillation parameters ([Stello et al. 2015](#)). We will see, however, that for some stars, additional measures are required to account for spectral window effects. We then calculate a power spectrum of the resulting light curve with a Lomb-Scargle periodogram ([Scargle 1982](#)).

Despite the efforts to remove systematic errors, the VJ light curves still exhibit non-negligible contamination at frequencies of $48.1\mu\text{Hz}$ and $46.3\mu\text{Hz}$ due to thruster firings. Generally, we do not find excess power at the nominal thruster firing frequency of $47.22\mu\text{Hz}$. [Figure 1](#) shows a median power spectrum across all GAP C1 spectra (8630 spectra in total) in a region around the thruster firing frequency. To calculate this spectrum, we

¹ <http://www.physics.usyd.edu.au/k2gap/>
<https://archive.stsci.edu/prepds/k2gap/>

² We exclude the Trans-Neptunian object, EPIC 200001049.

³ We do, however, identify red giants with solar-like oscillations at frequencies $\sim 3\mu\text{Hz}$, but the measured frequencies are upper limits and are not assigned errors.

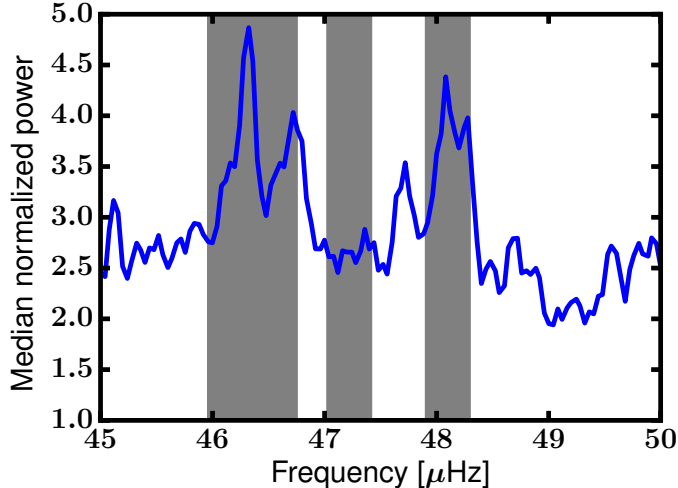


Figure 1. The median spectrum for all C1 objects. We identify two regions particularly affected by *K2* noise in VJ light curves: $46.3\mu\text{Hz} \pm 0.4\mu\text{Hz}$ (left) and $48.1\mu\text{Hz} \pm 0.2\mu\text{Hz}$ (right). The middle grey shaded region ($47.22\mu\text{Hz} \pm 0.2\mu\text{Hz}$) corresponds to the nominal thruster firing frequency of the spacecraft. These regions are treated specially in BAM, as described in the text.

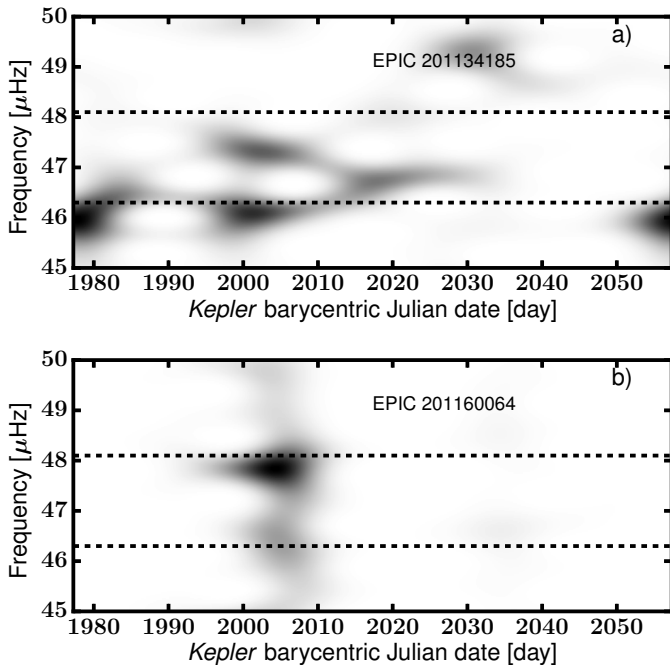


Figure 2. Two examples of a wavelet analysis of the same frequency range around the nominal thruster firing frequency as shown in Figure 1, for EPIC 201134185 (top) and EPIC 201160064 (bottom). Clearly the $48.1\mu\text{Hz}$ and $46.3\mu\text{Hz}$ instrumental features seen in the median spectrum (Fig. 1) are not necessarily both present in every light curve at the same level, and do not necessarily persist over the entire time baseline.

normalized each spectrum to the white noise level, defined to be the median power density in a range from $250\mu\text{Hz}$ to the Nyquist frequency of $283\mu\text{Hz}$.

In order to investigate whether the thruster firing noise features showed temporal variation over the course of the campaign, we computed a wavelet periodogram using the `astroML` library (Vanderplas et al. 2012). The chosen wavelet has the form

$$w(t, t_0, f_0, Q) \propto e^{-[f_0(t-t_0)/Q]^2} e^{2\pi i f_0(t-t_0)},$$

where t_0 and f_0 are the time and frequency of the 2D wavelet transform, t is the time coordinate for the entire baseline considered, and Q is a factor determining the time resolution of the wavelet transform: $Q \rightarrow \infty$ recovers a Fourier transform and $Q \rightarrow 0$ yields a wavelet periodogram with infinite temporal resolution. We set $Q = 30$ for analyzing the noise feature of interest, which allows for resolving features in time of approximately 1/10 the baseline of C1, i.e., 8 days.

Two representative wavelet periodograms for C1 are shown in Figure 2. We find that there are definite temporal structures in the frequency domain of the *K2* thruster firing noise. We note that C1 light curves reduced by Angus et al. (2016) also exhibit qualitatively similar features.

Given these noise features are present in most of the VJ light curves, we remove the affected regions of the power spectra in Fourier space by replacing each frequency bin in $0.2\mu\text{Hz}$ -wide regions on either side of $47.2\mu\text{Hz}$ and $48.1\mu\text{Hz}$, and a $0.4\mu\text{Hz}$ -wide region on either side of $46.3\mu\text{Hz}$. We replace the power density in this region with power drawn from a chi-square distribution scaled to a linear interpolation between the median power in regions $5\mu\text{Hz}$ on either side of the affected regions.

3. METHODS

After the pre-processing of the power spectrum with power, $A_o(\nu_j)$, at discrete frequencies, ν_j , which constitutes our data, D , we then fit a smooth background component to the power spectrum, whose sets of parameters, θ_{meso} and θ_{gran} , are used as guesses for a subsequent stage of determining the global asteroseismic parameter ν_{max} and the other parameters describing the oscillation excess, θ_{excess} , which is finally used to guide fitting the global asteroseismic parameters related to $\Delta\nu$, $\theta_{\Delta\nu}$.

We discuss each step in turn below.

3.1. Granulation calculation

BAM first fits a two-component Harvey-like model that Kallinger et al. (2014) find best describes the smooth background component of *Kepler* red giant

power spectra:

$$A(\nu_j) = \left[W_N(\nu_j) \text{sinc} \left(\frac{\pi}{2} \frac{\nu_j}{\nu_{\text{Nyq}}} \right) \right]^2 \sum_{i=1,2} \frac{\sigma_i^2 \tau_i}{1 + (\pi \nu_j \tau_i)^4} + \text{WN} \quad (1)$$

$$= A_{\text{meso}}(\nu_j) + A_{\text{gran}}(\nu_j) + \text{WN}, \quad (2)$$

where WN represents a white noise term, which will dominate red giant power spectra at high frequencies; σ_i are amplitudes of each so-called Harvey components; and τ_i are their characteristic time-scales. $A_{\text{meso}}(\nu_j)$ and $A_{\text{gran}}(\nu_j)$ are defined here to be the two Harvey components of the granulation background. The sinc pre-factor with dependence on the Nyquist frequency, ν_{Nyq} , arises due to $K\mathcal{L}$'s finite exposure times, and $W_N(\nu_j)$ is the spectral window function (see Kallinger et al. 2014 for more details).

Of the two Harvey-like components, the component at higher frequency is attributed to granulation, whereby the integrated light from the stellar disk varies due to convective cell brightness variations. The lower-frequency component is attributed to meso-granulation, which is likely due to the variation in convective cell brightness for cells with sizes around 5 – 10 times that of granular cells (for a review of convection on the stellar surface, see Nordlund et al. 2009). For bookkeeping purposes, we require that the second component always be identified with the granulation background for which $\tau_{\text{meso}} > \tau_{\text{gran}}$ and $\sigma_{\text{gran}}^2 \tau_{\text{gran}} < \sigma_{\text{meso}}^2 \tau_{\text{meso}}$.

We achieve a robust fit to the granulation background by taking advantage of scaling relations between ν_{max} and the granulation parameters (σ and τ) noted by previous work (e.g., Kjeldsen & Bedding 2011; Kallinger et al. 2010). These relations naturally translate into priors in a Bayesian framework. We construct priors on the granulation parameters as detailed in Table 1. The final prior for a set of trial parameters is the product of the individual priors according to:

$$\begin{aligned} P(\theta_{\text{meso}} = \{\sigma_{\text{meso}}, \tau_{\text{meso}}\}, \theta_{\text{gran}} = \{\sigma_{\text{gran}}, \tau_{\text{gran}}\}, \theta_{\text{excess}}) \\ &= P(\sigma_{\text{meso}} | \tau_{\text{meso}}, \sigma_{\text{gran}}, \tau_{\text{gran}} | \theta_{\text{excess}}) \\ &P(\tau_{\text{meso}}, \tau_{\text{gran}} | \sigma_{\text{gran}}, \theta_{\text{excess}}) P(\sigma_{\text{gran}} | \theta_{\text{excess}}) P(\theta_{\text{excess}}) \\ &= P(\sigma_{\text{meso}} | \nu_{\text{max}}) P(\tau_{\text{meso}} | \nu_{\text{max}}) P(\tau_{\text{gran}} | \nu_{\text{max}}) P\left(\frac{\tau_{\text{meso}}}{\tau_{\text{gran}}}\right) \\ &P(\sigma_{\text{gran}} | \nu_{\text{max}}), \end{aligned} \quad (3)$$

for which we introduce the notation θ_{excess} to indicate parameters describing the solar-like oscillations (as distinguished from the granulation parameters), and whose parameters (other than ν_{max}) are defined later. The granulation priors are conditional upon ν_{max} , and, in

this sense, ν_{max} is a latent variable that defines the relationships among all the granulation parameters.

Subsequently, we define a posterior probability given by

$$\begin{aligned} P(\theta_{\text{meso}}, \theta_{\text{gran}} | D = \{(\nu_j, A_o(\nu_j)), j = 0, 1, 2, \dots\}, \theta_{\text{excess}}) \\ \propto P(\theta_{\text{meso}}, \theta_{\text{gran}} | \theta_{\text{excess}}) \prod_j \left[\frac{1}{A(\nu_j)} \exp \left(-\frac{A_o(\nu_j)}{A(\nu_j)} \right) \right]. \end{aligned} \quad (4)$$

Here, $A_o(\nu_j)$ is the observed spectral density and $A(\nu_j)$ is the model given by Equation 2. Note that the above expression assumes χ^2 statistics and not Gaussian statistics to describe $A_o(\nu_j)/A(\nu_j) \sim \chi^2(2)$, where the observed spectrum is critically-sampled and the observed spectrum is modeled by $A(\nu_j)$.

Given a Bayesian model for the data, we explore the parameter space with Monte Carlo Markov Chains (MCMC), as implemented in `emcee` (Foreman-Mackey et al. 2013), and report best-fitting parameters as the median of their marginalized posterior distributions, and the uncertainty as the average of the range around the median encompassing 64% of the distribution. Of course, the prior factor, $P(\theta_{\text{meso}}, \theta_{\text{gran}} | \theta_{\text{excess}})$ depends on ν_{max} (see Table 1). We simultaneously fit for ν_{max} and the background parameters, with a guess for ν_{max} calculated from a smoothed version of the spectrum, as in the SYD pipeline (Huber et al. 2009). Note that in this step, the region of power excess is not explicitly modeled, and so ν_{max} is implemented effectively as a dummy variable for this granulation model fitting stage of the process. The resulting best-fitting parameters are then used as initial guesses for a more complicated model that adds an additional component to describe the oscillation excess power, which we describe next.

Ultimately, BAM allows the user to choose which of the priors listed in Table 1 are to be used. The results presented in this paper do not use the first four priors of Table 1 for this granulation background fitting step, though they are used for the subsequent fitting step that determines ν_{max} and A_{max} , as described in the next section. The extent to which the priors in Table 1 are applied does not significantly affect the resulting ν_{max} value.

3.2. ν_{max} and A_{max} calculation

In the subsequent step, we add another component to the model such that

$$A_{\text{tot}}(\nu_j) = A_{\text{meso}}(\nu_j) + A_{\text{gran}}(\nu_j) + A_{\text{excess}}(\nu_j) + \text{WN}, \quad (5)$$

where A_{excess} represents the power excess from solar-like oscillations, and $A_{\text{meso}}(\nu_j)$, $A_{\text{gran}}(\nu_j)$, and WN are

Parameter	Prior Distribution	Use
$\ln \sigma_{\text{gran}}$	$\mathcal{N}(-0.609 \ln \nu_{\text{max}} + 8.70, 0.165)$	Eq. 4 & Eq. 8
$\ln \tau_{\text{gran}}$	$\mathcal{N}(-0.992 \ln \nu_{\text{max}} - 1.09, 0.0870)$	Eq. 4 & Eq. 8
$\ln \sigma_{\text{meso}}$	$\mathcal{N}(-0.609 \ln \nu_{\text{max}} + 8.70, 0.165)$	Eq. 4 & Eq. 8
$\ln \tau_{\text{meso}}$	$\mathcal{N}(-0.970 \ln \nu_{\text{max}} + 0.00412, 0.970)$	Eq. 4 & Eq. 8
$\ln \frac{\tau_{\text{meso}}}{\tau_{\text{gran}}}$	$\mathcal{N}(1.386, 0.316)$	Eq. 4 & Eq. 8
$\ln b$	$\mathcal{N}(1.05 \ln \nu_{\text{max}} - 1.91, 0.198)$	Eq. 8
$\ln A_{\text{max}} + \ln b$	$\mathcal{N}(-1.32 \ln \nu_{\text{max}} + 14.5, 1.22)$	Eq. 8

Table 1. Priors used for the full power spectrum fit, Equation 8, adapted from Kallinger et al. (2010). The notation $\mathcal{N}(a, b)$ indicates a Gaussian distribution with mean a and standard deviation b . Whether or not a given prior enters into Equation 4 or Equation 8 is indicated in the final column.

defined in Equation 2. We model A_{excess} as a Gaussian profile

$$A_{\text{excess}} = A_{\text{max}} \left[W_N(\nu_j) \text{sinc} \left(\frac{\pi}{2} \frac{\nu_j}{\nu_{\text{Nyq}}} \right) \right]^2 \exp \left[-\frac{(\nu_j - \nu_{\text{max}})^2}{2b^2} \right] \quad (6)$$

Our prior is now:

$$\begin{aligned} P(\theta_{\text{meso}}, \theta_{\text{gran}}, \theta_{\text{excess}} = \{A_{\text{max}}, \nu_{\text{max}}, b\}) &= \\ &P(\sigma_{\text{meso}} | \tau_{\text{meso}}, \tau_{\text{gran}}, \sigma_{\text{gran}}, \theta_{\text{excess}}) \\ &P(\tau_{\text{meso}}, \tau_{\text{gran}} | \sigma_{\text{gran}}, \theta_{\text{excess}}) P(\sigma_{\text{gran}} | \theta_{\text{excess}}) P(\theta_{\text{excess}}) \\ &= P(\sigma_{\text{meso}} | \nu_{\text{max}}) P(\tau_{\text{meso}} | \nu_{\text{max}}) P(\tau_{\text{gran}} | \nu_{\text{max}}) P\left(\frac{\tau_{\text{meso}}}{\tau_{\text{gran}}}\right) \\ &P(\sigma_{\text{gran}} | \nu_{\text{max}}) P(b, A_{\text{max}}, \nu_{\text{max}}) \\ &= P(\sigma_{\text{meso}} | \nu_{\text{max}}) P(\tau_{\text{meso}} | \nu_{\text{max}}) P(\tau_{\text{gran}} | \nu_{\text{max}}) P\left(\frac{\tau_{\text{meso}}}{\tau_{\text{gran}}}\right) \\ &P(\sigma_{\text{gran}} | \nu_{\text{max}}) P(b | \nu_{\text{max}}) P(A_{\text{max}}, b | \nu_{\text{max}}). \end{aligned} \quad (7)$$

We construct a posterior probability given by:

$$P(\theta_{\text{meso}}, \theta_{\text{gran}}, \theta_{\text{excess}} | D) \propto P(\theta_{\text{meso}}, \theta_{\text{gran}}, \theta_{\text{excess}}) \prod_j \left[\frac{1}{A_{\text{tot}}(\nu_j)} \exp \left(-\frac{A_o(\nu_j)}{A_{\text{tot}}(\nu_j)} \right) \right]. \quad (8)$$

In this case, the total prior is a product over all priors listed in Table 1. By first fitting the parameters of the granulation as described in §3.1 and subsequently using these as priors for the fit involving both the granulation model and the Gaussian excess, we reduce the burn-in time and the chance of getting stuck at local maxima. It will also make more convenient our oscillator selection process, described in §3.6.

3.3. Low frequency oscillators

We find that objects oscillating at frequencies $\nu_{\text{max}} \lesssim 15 \mu\text{Hz}$ exhibit significant spectral leakage at frequencies $30 \mu\text{Hz} \lesssim \nu \lesssim 100 \mu\text{Hz}$, often confusing the pipeline to fit ν_{max} at the location of the leakage, as shown in Figure 3a. We correct for this leakage at each step in our MCMC chains: for each trial model granulation spectrum (Eq. 2), we compute an amplitude spectrum, with each frequency in the spectrum being assigned a random spectral phase. This amplitude spectrum is then convolved with the spectral window, and squared to yield a power spectrum (see Murphy et al. 2013 for a worked example of how to contend with the spectral window in the context of asteroseismology, specifically). A lightly smoothed version of this convolved granulation power spectrum is added to the power excess term to create a model of the power spectrum that takes into account spectral leakage. This model is then fitted to the observed power spectrum within the Bayesian framework. Note that the trial power excess term is not convolved with the window function, as it turns out it adds minimally to the spectral leakage compared to the granulation background, and it can lead to unstable fits in which the entire spectrum is modeled as a Gaussian excess plus its resulting spectral leakage. We find that this procedure results in correct ν_{max} identifications for $\nu_{\text{max}} \lesssim 15$. Correcting for spectral leakage results in a statistically significant difference in fitted granulation parameters for low frequency oscillators (Fig. 3b; note difference in shape of blue curve in regions dominated by granulation).

A caveat for these stars is that the lowest ν_{max} ($\nu_{\text{max}} \lesssim 4 \mu\text{Hz}$) values likely represent upper limits for ν_{max} because the $K2$ resolution prevents an unambiguous determination of ν_{max} . Indeed, at frequencies near $\sim 3 \mu\text{Hz}$, there may only be three modes visible (e.g., Stello et al. 2014), which limits the precision with which a central ν_{max} may be defined using the Gaussian to model oscillation excess (Eq. 6).

3.4. $\Delta\nu$ calculation

We furthermore take advantage of the correlation between ν_{max} and $\Delta\nu$ to place a prior on $\Delta\nu$ in the same way we place priors on granulation parameters described in §3.1 & §3.2. Because of the short duration of $K2$ light curves (~ 80 days), individual modes may not be well-resolved, and therefore the large frequency separation can be difficult to measure. BAM measures $\Delta\nu$ in two independent ways: one using the SYD autocorrelation method (see Huber et al. 2009), and the other using the $\Delta\nu$ -folded power spectrum centered around ν_{max} and extending on $3\Delta\nu$ on either side, as shown in Figure 4.

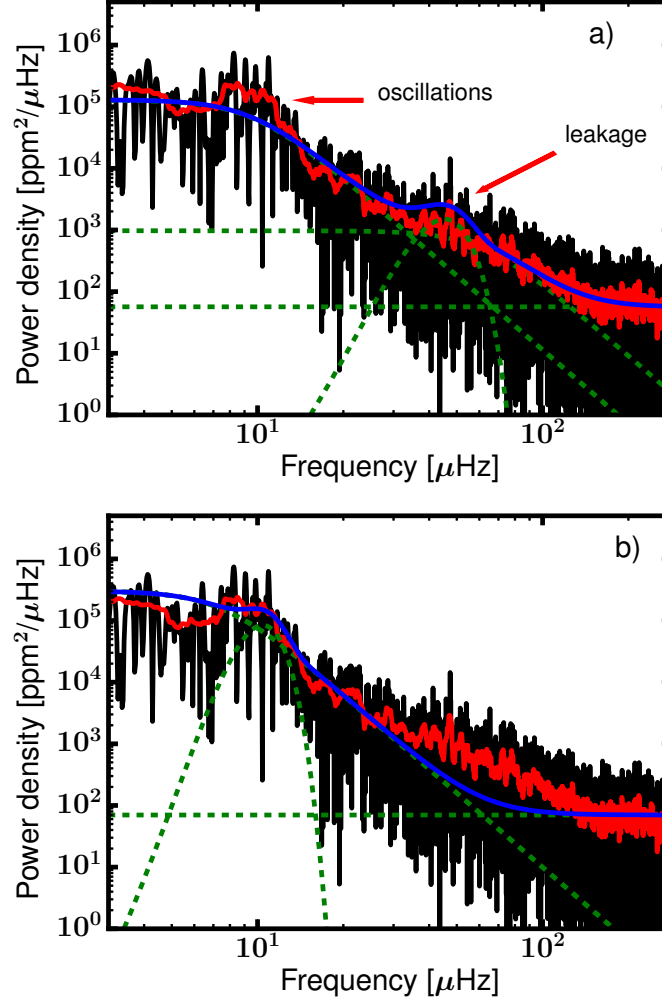


Figure 3. Raw (black) and smoothed (red) power spectrum of EPIC 201186616, and model fits without (a) and with (b) spectral window corrections (blue). Each component of the models is shown in green dashed curves (white noise, Gaussian excess, and Harvey components). The meso-granulation component does not contribute significantly to the fit upon spectral window correction, and so is not shown in (b).

Parameter	Prior Distribution
δ_{01}	$\mathcal{N}(-0.025\Delta\nu^a, 0.1\Delta\nu^b)$
δ_{02}	$\mathcal{N}(0.121\Delta\nu^a + 0.047^a, 0.1\Delta\nu^b)$
A_0	$\mathcal{N}(1.0^c, 0.15^b)$
A_1	$\mathcal{N}(0.5^c, 0.15^b)$
A_2	$\mathcal{N}(0.8^c, 0.15^b)$
FWHM ₀	$\mathcal{U}(0.035\Delta\nu_{\text{guess}}^b, 0.45\Delta\nu_{\text{guess}}^b)$
FWHM ₁	$\mathcal{U}(0.035\Delta\nu_{\text{guess}}^b, 0.9\Delta\nu_{\text{guess}}^b)$
FWHM ₂	$\mathcal{U}(0.035\Delta\nu_{\text{guess}}^b, 0.45\Delta\nu_{\text{guess}}^b)$
$\Delta\nu$	$\mathcal{N}(\Delta\nu_{\text{guess}}^b, 0.15^b\Delta\nu_{\text{guess}}^b)$
C	$\mathcal{U}(0.001^b, 0.1^b)$

Table 2. Priors used for the fit to $\Delta\nu$, Equation 9. The notation $\mathcal{U}(a, b)$ indicates a uniform distribution between a and b . Priors adapted from Huber et al. (2010)^a; Current work^b; and Stello et al. (2016)^c. $\Delta\nu_{\text{guess}}$ is the expected $\Delta\nu$ given a ν_{max} , from Stello et al. (2009): $\Delta\nu_{\text{guess}} \equiv 0.263\nu_{\text{max}}^{0.772}$.

The background contribution from the Harvey components of the model are divided out, and the folded power spectrum is computed by folding the spectrum on $\Delta\nu$, where each bin of the folded spectrum contains the sum over the power by folding the spectrum $3\Delta\nu$ on either side of ν_{max} by $\Delta\nu$; the bins are then normalized such that the highest peak of the folded power spectrum is unity. For the majority of red giants the folded spectrum shows three broad oscillation power excess regions corresponding to the radial, dipole, and quadrupole modes. We do not fit an octopole mode component because its low power usually makes it undetectable in $K2$ data. We obtain $\Delta\nu$ from this diagram by modeling it using three Lorentzian profiles, appropriate for solar-like oscillation modes, corresponding to the radial ($\ell = 0$), dipole

($\ell = 1$), and quadrupole ($\ell = 2$) modes, as follows :

$$A_{\text{folded}}(\nu_j, (\nu_\ell, A_\ell, \text{FWHM}_\ell)_{\ell=0,1,2}, \Delta\nu, C) = \sum_{\ell=0}^{\ell=2} \frac{A_\ell}{1.0 + \frac{[(\nu_j \bmod \Delta\nu) - \nu_\ell]^2}{\text{FWHM}_\ell^2/4}} + C. \quad (9)$$

C is a constant to model the imperfections when removing the background level in the vicinity of ν_{max} . The frequencies of the modes, ν_ℓ , in the folded central power spectrum are given by :

$$\begin{aligned} \nu_0 &\equiv \epsilon \\ \nu_1 &= \nu_0 - \frac{1}{2}\Delta\nu + \delta\nu_{01} \\ \nu_2 &= \nu_0 - \delta\nu_{02}. \end{aligned}$$

The positions of the non-radial modes with respect to the radial mode, ϵ , thus follow standard definitions (e.g., [Bedding & Kjeldsen 2010](#)), such that a given mode in the spectrum has a frequency, ν , given by $\nu \approx \Delta\nu(n + \ell/2 + \epsilon)$, where n is the radial order of the mode.

Placing priors on the above parameters as detailed in [Table 2](#) following the procedure in [§3.1](#) & [§3.2](#) of the form

$$\begin{aligned} P(\theta_{\Delta\nu} = \{(\delta_{01}, \delta_{02}), (A_0, A_1, A_2), \\ (\text{FWHM}_0, \text{FWHM}_1, \text{FWHM}_2), \Delta\nu, C\} | \theta_{\text{excess}}) \\ &= P((\delta_{01}, \delta_{02}), (A_0, A_1, A_2), \\ &(\text{FWHM}_0, \text{FWHM}_1, \text{FWHM}_2), \Delta\nu | b, A_{\text{max}}, \nu_{\text{max}}) \\ &= P((\delta_{01}, \delta_{02}) | \nu_{\text{max}}) P((A_0, A_1, A_2) | \nu_{\text{max}}) \\ &P((\text{FWHM}_0, \text{FWHM}_1, \text{FWHM}_2) | \nu_{\text{max}}) P(\Delta\nu | \nu_{\text{max}}) \end{aligned}$$

yields a posterior probability

$$P(\theta_{\Delta\nu} | D, \theta_{\text{excess}}) \propto P(\theta_{\Delta\nu} | \theta_{\text{excess}}) \prod_j \left[\frac{A_{\text{o,folded},j}(\nu_j, \Delta\nu)^{n_j-1}}{A_{\text{folded},j}(\nu_j, \theta_{\Delta\nu})^{n_j}} \exp\left(-n_j \frac{A_{\text{o,folded}}(\nu_j, \Delta\nu)}{A_{\text{folded}}(\nu_j, \theta_{\Delta\nu})}\right) \right] \quad (10)$$

where we use the statistics for an averaged spectrum derived in [Appourchaux \(2003\)](#). $A_{\text{o,folded}}(\nu_j, \Delta\nu)$ is the power at frequency bin ν_j in the observed folded spectrum for a given $\Delta\nu$, and is a function of $\Delta\nu$: depending on $\Delta\nu$, the folding process will distribute the power in frequency bins, $A_{\text{o,folded}}(\nu_j, \Delta\nu)$, differently. In practice what this requires is re-computing the folded spectrum for each trial $\Delta\nu$ in our MCMC. $A_{\text{folded}}(\nu_j, \theta_{\Delta\nu})$ is the model for the folded spectrum (Eq. 9), and n_j is the number of points that went into the sum over power for that bin in the folded power spectrum.

Using the folded spectrum is particularly useful for determining $\Delta\nu$ from *K2* data because individual mode

frequencies are not very well resolved. What complicates the recovery of $\Delta\nu$ in the presence of degraded spectral resolution is that observed mode amplitudes and phases (and hence frequencies) are not stable with time, and have intrinsic scatter. This is because the oscillations are stochastically-driven and damped (e.g., [Woodard 1984](#)), which causes continuous variation in the centroid of mode frequencies and their amplitudes. The random behavior of the stochastic mode profile can only be mitigated by averaging spectra that are independent in frequency or in time (for a review of power spectrum statistics in the context of solar-like oscillations, see [Anderson et al. 1990](#), and references therein). The folded spectrum approach therefore effectively averages out the random behavior of the modes and increases their signal-to-noise, and is what would be called an ‘*m*-averaged’ spectrum ([Anderson et al. 1990](#)) in the context of solar modes.

To find the optimal $\Delta\nu$, we start with a guess value derived from the $\Delta\nu$ - ν_{max} relation by [Stello et al. \(2009\)](#)

$$\Delta\nu_{\text{guess}} = 0.263\nu_{\text{max}}^{0.772}. \quad (11)$$

We determine best-fitting values by MCMC, in which $\Delta\nu$ is constrained to be $0.7\Delta\nu_{\text{guess}} < \Delta\nu < 1.3\Delta\nu_{\text{guess}}$ and apply priors as described in [Table 2](#). BAM returns $\Delta\nu$ values for stars for which there is agreement to within 2σ with $\Delta\nu$ computed using the SYD autocorrelation method and for which the uncertainty on $\Delta\nu$ is less than the spread in the $\Delta\nu$ prior. The latter requirement captures information about how reliably the modes have been fit, and serves as a means of determining which stars have more information about $\Delta\nu$ than our prior choice. Note that BAM’s second, separate $\Delta\nu$ value from an autocorrelation approach acts as a sort of second opinion. This autocorrelation $\Delta\nu$ will not in general be the same $\Delta\nu$ that a stand-alone application of the SYD pipeline to the same star would: the autocorrelation method requires a ν_{max} to identify the region of the power spectrum that contains the power excess, and it also requires a removal of the smooth background of the power spectrum, both of which are independent of SYD in this case (for details of the autocorrelation approach to calculating $\Delta\nu$, see [Huber et al. 2009](#)). We show an example of a model fit to the folded spectrum from this process in [Figure 4](#).

Importantly, the priors that are placed on $\Delta\nu$ are not too stringent. We tested the sensitivity of our $\Delta\nu$ results on priors by increasing the spread in the $\Delta\nu$ prior to $0.9\Delta\nu_{\text{guess}}$ from $0.15\Delta\nu_{\text{guess}}$ (see [Table 2](#)). For confirmed oscillators in the C1 *K2* GAP sample, our best-fitting $\Delta\nu$ values are not significantly different when us-

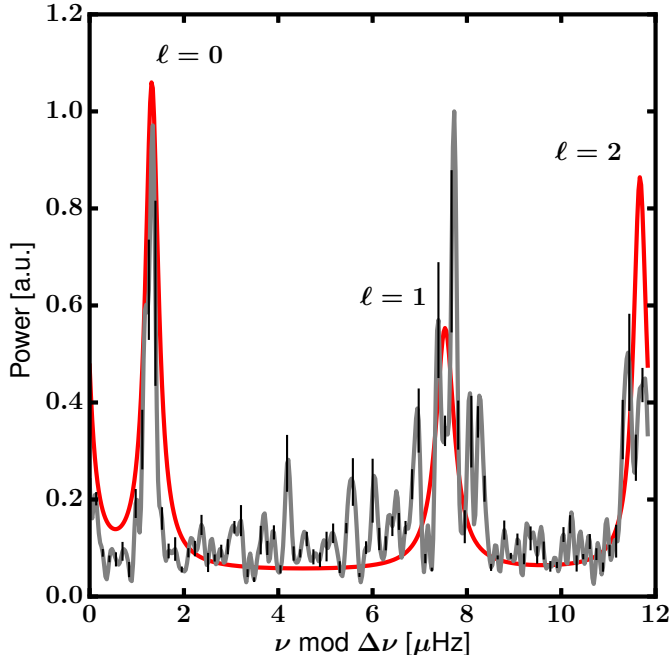


Figure 4. An example fit by BAM to the folded central power spectrum, with best-fitting model (red) and data (grey); black error bars are calculated as described in the text, of which every 5th is shown, for clarity.

ing our fiducial prior or a widened prior. We show the difference in best-fitting $\Delta\nu$ using these two different priors in Figure 5. The spread is less than 0.1σ for the majority of objects, indicating that the priors indeed do not significantly impact the determination of $\Delta\nu$.

3.5. Comparison to SYD

BAM parameters agree favorably with those computed by other techniques via different pipelines, as demonstrated in (Stello et al. 2017). As a point of comparison to a well-established asteroseismic pipeline, Figure 6 shows BAM ν_{\max} and $\Delta\nu$ values compared to those from SYD for the C1 GAP oscillator sample. The BAM parameters for this comparison exercise have been re-derived using slightly different methodology than described in the GAP Data Release 1 (GAP DR1) release paper (Stello et al. 2017) so as to be consistent with the methodology presented in this work. SYD values for $\Delta\nu$ and ν_{\max} are taken directly from GAP DR1. Only giants candidates that were verified to be such by eye in Stello et al. (2017) and that BAM selects as giants according to §3.6 are considered in this comparison exercise.

The median in the normalized distribution of differences between BAM and SYD $\Delta\nu$ values for this GAP comparison sample (solid black vertical line in Figure 6b) indicates a systematic offset of $\sim 0.6\%$. The red histogram in Figure 6b shows the $\Delta\nu$ differences dis-

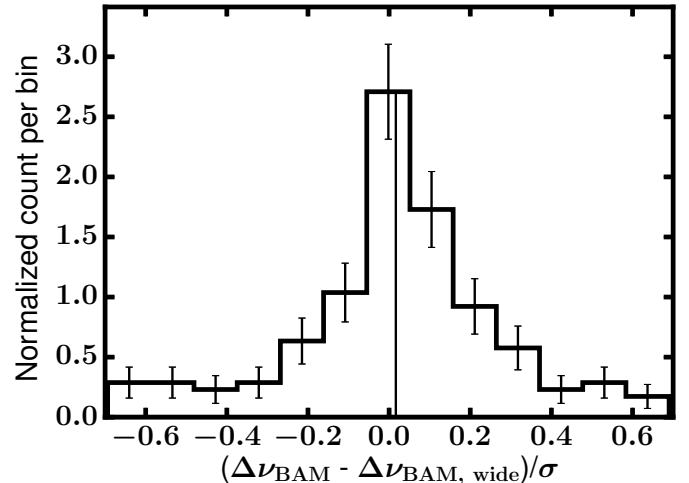


Figure 5. The difference in best-fitting $\Delta\nu$ when using a $\Delta\nu$ prior of width $0.9\Delta\nu_{\text{guess}}$ ($\Delta\nu_{\text{BAM, wide}}$) versus the nominal $0.15\Delta\nu_{\text{guess}}$, normalized by the error in the difference, σ ; error bars on the histogram bins correspond to Poisson uncertainties. The vertical line corresponds to the median of the distribution. This indicates that the differences between BAM runs with an expanded prior on $\Delta\nu$ results in insignificant differences — 10 times smaller than the error on $\Delta\nu$ — in the resulting $\Delta\nu$.

tribution if the BAM values are re-scaled downward by 0.6%, which brings the distribution into better alignment with the expected Gaussian. The median in the distribution of ν_{\max} differences indicates a marginally significant (1σ) systematic offset between the two ν_{\max} scales (solid black vertical line in Figure 6a), and which corresponds to a difference in BAM and SYD ν_{\max} scales of $\sim 0.2\%$. There does appear to be an under-estimation of either BAM or SYD $\Delta\nu$ values (black histogram in Figure 6a), which is ameliorated by re-scaling the error on the difference upward by 30% (red histogram in Figure 6a).

Given that Kallinger et al. (2014) found systematic differences of up to $\sim 5\%$ in ν_{\max} depending on the model used for the meso-granulation and granulation background, any small systematic difference in ν_{\max} could easily be due to the different treatment of the background between BAM and SYD. For example, the sinc term in Equation 2 is not included in the SYD pipeline. This difference in methodology could plausibly explain the 0.6% systematic difference in $\Delta\nu$, as well: the positions of the modes used to measure $\Delta\nu$ will be affected by the choice of the meso-granulation and granulation background, which are removed before calculating the folded spectrum.

Apart from these systematic differences, we find BAM parameters are consistent with SYD to within $\sim 1.53\%$

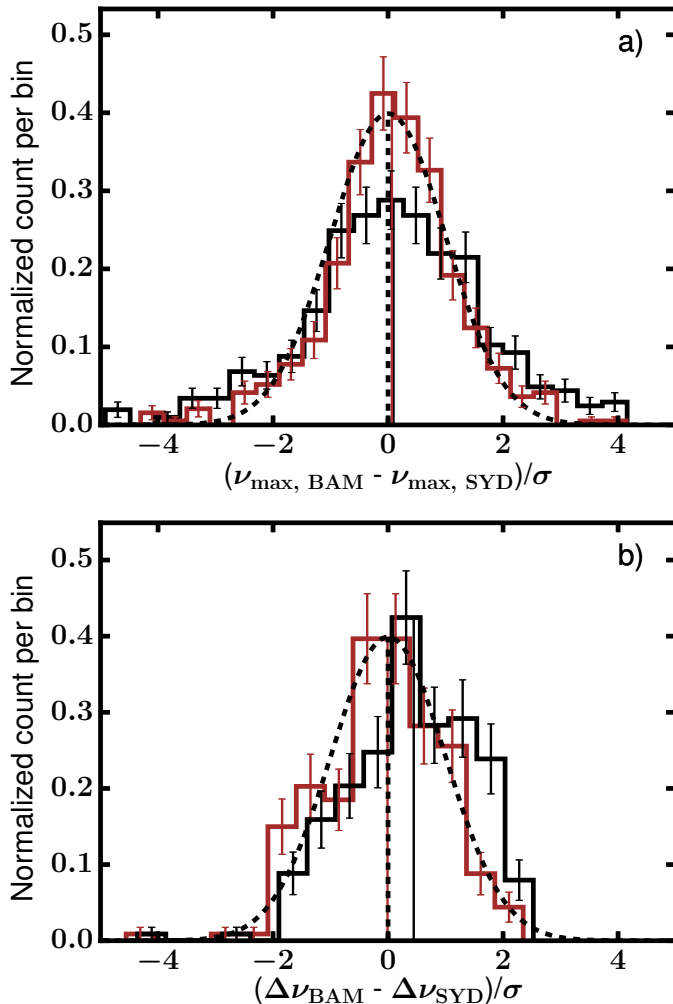


Figure 6. Distributions of the differences between BAM and SYD ν_{\max} (a) and $\Delta\nu$ (b), normalized by the sum in quadrature of their errors, $\sigma \equiv \sqrt{\sigma_{\nu_{\max, \text{BAM}}}^2 + \sigma_{\nu_{\max, \text{SYD}}}^2}$ and $\sigma \equiv \sqrt{\sigma_{\Delta\nu_{\text{BAM}}}^2 + \sigma_{\Delta\nu_{\text{SYD}}}^2}$. The medians of both distributions are shown as vertical, solid black lines; error bars on the histogram bins correspond to Poisson uncertainties. The red distributions in each panel indicate the distributions of differences in BAM and SYD values after systematic differences in central value and/or uncertainties are corrected, according to the text. The dotted curve is a Gaussian, to guide the eye; the vertical dashed line is centered at zero. Stars plotted here are drawn from the C1 GAP sample deemed from manual inspection to be definite oscillators (see Stello et al. 2017) and such that both SYD and BAM as implemented in this work returned ν_{\max} or $\Delta\nu$ values.

and 1.51% for ν_{\max} and $\Delta\nu$, which correspond to the BAM GAP sample mean fractional errors on ν_{\max} and $\Delta\nu$, respectively. There is some ambiguity as to the agreement in ν_{\max} , where the errors on ν_{\max} for either BAM or SYD may be under-estimated by up to 30%, given the non-Gaussianity of the ν_{\max} difference distri-

bution (black histogram in Figure 6a). Non-Gaussianity in comparisons across pipelines was also found in Stello et al. (2017), and in part is caused by under- and over-estimation of errors in *K2* asteroseismic parameters (Pinsonneault et al. 2018, Zinn et al., in prep.).

3.6. Bayesian oscillator selection

Because our approach for measuring the oscillation and granulation parameters will always provide a best-fitting model, even if there is no solar-like oscillation signal, we still need to determine if a fit corresponds to a true detection. As mentioned in §1, BAM’s Bayesian approach means that we can use the parameter fits to determine which stars are, and are not, true oscillators.

This is essentially a problem in model comparison: does the model with a power excess term (Equation 5) describe a star’s power spectrum better or does one without power excess (Equation 2)? Jeffreys (1935) first formalized model comparison in a Bayesian approach using what is now called the Bayes factor, defined to be the ratio of the posterior odds in favor of a model to its prior odds. The Bayes factor derives simply from Bayes theorem, by which the posterior odds of M_1 can be written as

$$\frac{P(M_1|D)}{P(M_2|D)} = \frac{P(D|M_1) P(M_1)}{P(D|M_2) P(M_2)}. \quad (12)$$

In our case, the probability densities, $P(D|M_1)$ and $P(D|M_2)$ correspond to integrals of Equations 8 & Equation 4 over all of parameter space, and we assume that, a priori, a star is as likely to be a non-oscillator as an oscillator, in which case the prior odds of M_1 , $\frac{P(M_1)}{P(M_2)} = 1$. The Bayes factor is defined as $B \equiv \frac{P(D|M_1)}{P(D|M_2)}$.

To compute the Bayes factor, one needs to integrate the conditional probability densities of Equations 8 & 4 over all of parameter space. Though these conditional probability densities share the same priors on granulation parameters, $P(\theta_{\text{meso}}, \theta_{\text{gran}} | \theta_{\text{excess}})$, they do not neatly cancel out when computing the Bayes factor because $P(D|M_1)$ and $P(D|M_2)$ in Equation 12 are each separate integrals involving these priors. Such integrals are often computationally expensive to do, and analytically intractable. Fortunately, there are various methods available to approximate the Bayes factor (e.g., Green 1995; Chib & Jeliazkov 2001; Skilling 2004). We use the widely-applicable Bayesian Information Criterion (WBIC; Watanabe 2013) to compute the Bayes factor. This method generalizes the Bayesian Information Criterion (Schwarz 1978), such that the WBIC approximates the Bayes factor in the limit of weak priors and

with the assumption that the posterior is asymptotically normal:

$$\ln B \approx \Delta_{\text{WBIC}} \equiv \langle \ln \mathcal{L}_1 \rangle_{P(\theta|D)} - \langle \ln \mathcal{L}_2 \rangle_{P(\theta|D)}, \quad (13)$$

where $\langle \rangle_{P(\theta|D)}$ indicates a mean taken over the modified posteriors of Equations 14 & 15 (see below), and the likelihoods are from Equations 8 & 4 ($\mathcal{L}_1 \equiv \prod_j \left[\frac{1}{A_{\text{tot}}(\nu_j)} \exp\left(-\frac{A_o(\nu_j)}{A_{\text{tot}}(\nu_j)}\right) \right]$ and $\mathcal{L}_2 \equiv \prod_j \left[\frac{1}{A(\nu_j)} \exp\left(-\frac{A_o(\nu_j)}{A(\nu_j)}\right) \right]$).

Crucially, the WBIC approach means that the Bayes factor can be computed trivially in a MCMC setting. We compute the means $\langle \ln \mathcal{L}_1 \rangle_{P(\theta|D)}$ and $\langle \ln \mathcal{L}_2 \rangle_{P(\theta|D)}$ using our two-step MCMC method, recalling that we perform fits to the data both with and without a power excess term (Equations 5 & Equation 2). For the purposes of approximating the Bayes factor, then, we run each MCMC an additional time, except using modified conditional posteriors so that instead of Equations 8 & 4, we have:

$$P(\theta_{\text{meso}}, \theta_{\text{gran}}, \theta_{\text{excess}}|D) \propto P(\theta_{\text{meso}}, \theta_{\text{gran}}, \theta_{\text{excess}}) \prod_j \left[\frac{1}{A_{\text{tot}}(\nu_j)} \exp\left(-\frac{A_o(\nu_j)}{A_{\text{tot}}(\nu_j)}\right) \right]^\beta \quad (14)$$

and

$$P(\theta_{\text{meso}}, \theta_{\text{gran}}|D = \{(\nu_j, A_o(\nu_j)), j = 0, 1, 2, \dots\}, \theta_{\text{excess}}) \propto P(\theta_{\text{meso}}, \theta_{\text{gran}}|\theta_{\text{excess}}) \prod_j \left[\frac{1}{A(\nu_j)} \exp\left(-\frac{A_o(\nu_j)}{A(\nu_j)}\right) \right]^\beta, \quad (15)$$

where $\beta \equiv 1/\ln N$, with N being the number of points in the power spectrum being fit. While performing a MCMC fit using posteriors from Equations 14 & 15 in place of Equations 8 & 4, we save the original likelihoods from Equations 8 & 4 at each link in our MCMC chains. In the end, we take an average of those likelihoods, insert into Equation 13, and in this way compute the Bayes factor.

We interpret the strength of evidence for the Gaussian excess model following Kass (1995), who recommend that $\ln B > 1$ would indicate positive evidence for the Gaussian excess model. We also require that the granulation component be resolved by imposing that the white noise be lower than the granulation component power (i.e., that the white noise should not dominate

the power spectrum). Note that these selection criteria do not include information about $\Delta\nu$: identifying excess power corresponding to ν_{max} is easier than identifying $\Delta\nu$, especially in the presence of mixed modes exhibited in red clump stars. The sample of non-GAP red giants that we will discuss in §4 are these candidates that had evidence according to the Bayes factor of exhibiting solar-like oscillations ($\ln B > 1$): 316 giant candidates are chosen in this way from the non-GAP sample of 13016 objects.

For every star in this sample of oscillating red giant candidates, we confirmed BAM’s selections as bona fide giants or not by visual inspection of the power spectra. We categorized each of BAM’s giant candidates into one of three categories: as having 1) a spectrum with oscillation modes that are discernible individually by eye or with excess power that is conspicuous by eye (‘yes’ oscillator); 2) a spectrum with marginal evidence of excess power at a frequency consistent with the shape of the granulation and meso-granulation components (‘maybe’ oscillator); or 3) a spectrum that shows at best very weak evidence of excess power or whose model power spectrum is in clear disagreement with the observed one (‘no’ oscillator). The ν_{max} inferred by eye in the ‘yes’ and ‘maybe’ cases must be within $3\mu\text{Hz} - 283\mu\text{Hz}$, such that giants that show evidence of a granulation spectrum at low frequencies are not selected as oscillators if the power excess is not visible above $3\mu\text{Hz}$. In this discernment process, the amplitude of the power spectrum, which has a relation to ν_{max} (as formalized, e.g., in Kallinger et al. 2014 and in Table 1), is allowed to be 10-50 times smaller than might be expected of a giant, to allow for cases where light from a non-oscillator contaminates the light curve, hence reducing the fractional brightness variation from granulation and oscillations. This effect can be significant. For instance, if a foreground dwarf of the same brightness as a background giant falls on the giant’s aperture mask, it would dilute the signal of the giant’s power spectrum by a factor of four.

Upon this visual verification, 31 of BAM’s non-GAP giant candidates were certain oscillators; 73 possible oscillators; and 212 not oscillating giants.

4. RESULTS AND DISCUSSION

We apply the BAM pipeline to 13016 C1 targets with VJ light curves not in the GAP sample, which have been selected for a wide range of science programs—mostly detection of planets around dwarfs. We identify 31 red giants that have detectable oscillation excesses that satisfy the BAM selection criteria of §3.6 and that have been validated by individual inspection — 21 of these

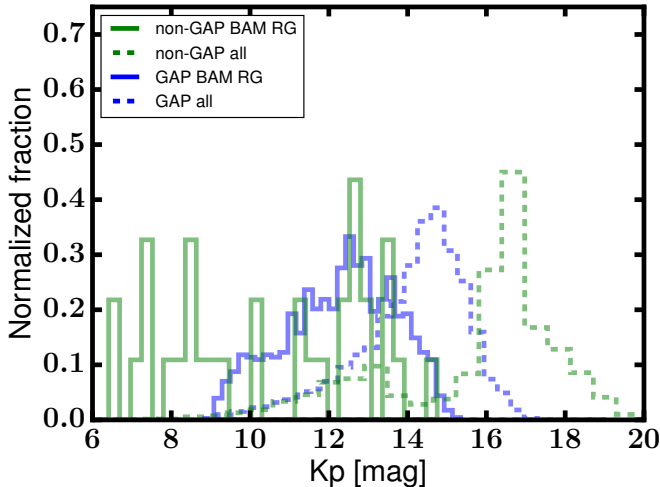


Figure 7. Magnitude distribution of the BAM non-GAP giant sample of this work (solid green line), compared to all observed non-GAP C1 targets (dashed green line); all GAP targets (dashed blue line); and GAP oscillators from [Stello et al. \(2017\)](#) (solid blue line).

are from GO proposal target lists that did not intentionally target giants. An additional 73 objects are potential giants, though can not be definitely confirmed as such. 70 of these ‘maybe’ cases are from programs that did not intentionally target giants. Combined, these 104 red giants and red giant candidates represent an 8% increase in the number of giants identified from C1 compared to those from the GAP sample [Stello et al. \(2017\)](#), which expressly targeted giants. The global oscillation parameters and granulation parameters for the red giants and red giant candidates are given in Table 3.

4.1. Completeness and purity of observed non-GAP giants

The magnitude distribution of the stars we find in this serendipitous sample, shown in Figure 7, demonstrates that BAM can recover red giant oscillations in *K2* down to $Kp \sim 14$ ($H \sim 12$). All the adopted magnitudes and colors we use in the following are taken from the Ecliptic Input Catalogue (EPIC; [Huber et al. 2016](#)).⁴ Note that even though the majority of the non-GAP C1 targets have $Kp \gtrsim 15$ (dashed green), the non-GAP giant sample from this work mostly has $Kp \lesssim 15$ (solid green). This is due to white noise dominating the spectra of giants at fainter magnitudes, and is the reason why the

⁴ A few objects had photometry in the EPIC that did not correspond to the giant in question, and these mismatches were corrected by searching for the nearest, brighter neighbor in the EPIC. The EPIC IDs affected were 201269306, 201472519, and 201724514.

number of GAP giants also drops beyond $Kp \gtrsim 13$ (solid blue). We adopt a conservative $Kp = 13$ as our fiducial completeness limit, whose actual completeness we will test in the next section by comparing to a model of the C1 non-GAP oscillators.

The purity of the non-GAP giant sample from BAM can be thought of as how many giants are verified visually as giants out of all the candidates that BAM believes are giants (i.e., 31 out of 316). Given that the majority of the non-GAP targets were selected by GO programs to be dwarfs, it is unsurprising that there are giant impostors that BAM mistakenly selected as giant candidates. Encouragingly, we find that BAM does not mistake the power in the frequency spectra from *K2*’s regular thruster firing for genuine oscillator excess. Instead, the objects mistakenly flagged as oscillators are due to one of a handful of failure modes. A full half of the false positives are objects exhibiting sharp, periodic signals overlaid on smooth, power-law spectra. Unlike genuine solar-like oscillators, however, objects falling into the latter failure mode generally exhibit multiple peaks (e.g., in Figure 8a). In future work, power spectra of periodic signals could be separated from those of giants by adding a second power excess component in Equation 5. If the best-fitting model preferred two regions of power excess instead of one, the spectrum would be rejected as a possible periodic case and not a giant. The other half of the false positives are either borderline ‘maybe’/‘no’ cases where the power excess is seemingly absent, but a granulation signal is present; cases in which BAM has converged on an incorrect ν_{\max} (in which case, even if the giant is oscillating, it is assigned a ‘no’ category); or dwarfs that have enough low-frequency activity to mimic a noisy giant granulation spectrum. Examples of these false positives are shown in Figures 8a&b, in addition to an example of a potential giant oscillator (Figure 8c) and examples of bona fide oscillators (Figures 8d-f).

To get a better idea of the completeness of the sample, and to better understand the distributions of the observed properties of the non-GAP giant sample, we compare to a simulation that we describe in the next section.

4.2. *Galaxia* simulation of non-GAP giants

We model the non-GAP giant population using a *Galaxia* synthetic population of all stars in the field of Campaign 1 (see [Sharma et al. 2011](#) for a description of *Galaxia* and [Stello et al. 2017](#) for a comparison of this synthetic population to observed asteroseismic red giants from the GAP targets). Non-GAP *Galaxia* giants are defined to have $3\mu\text{Hz} < \nu_{\max} < 290\mu\text{Hz}$, $Kp < 13$, and a probability of detection

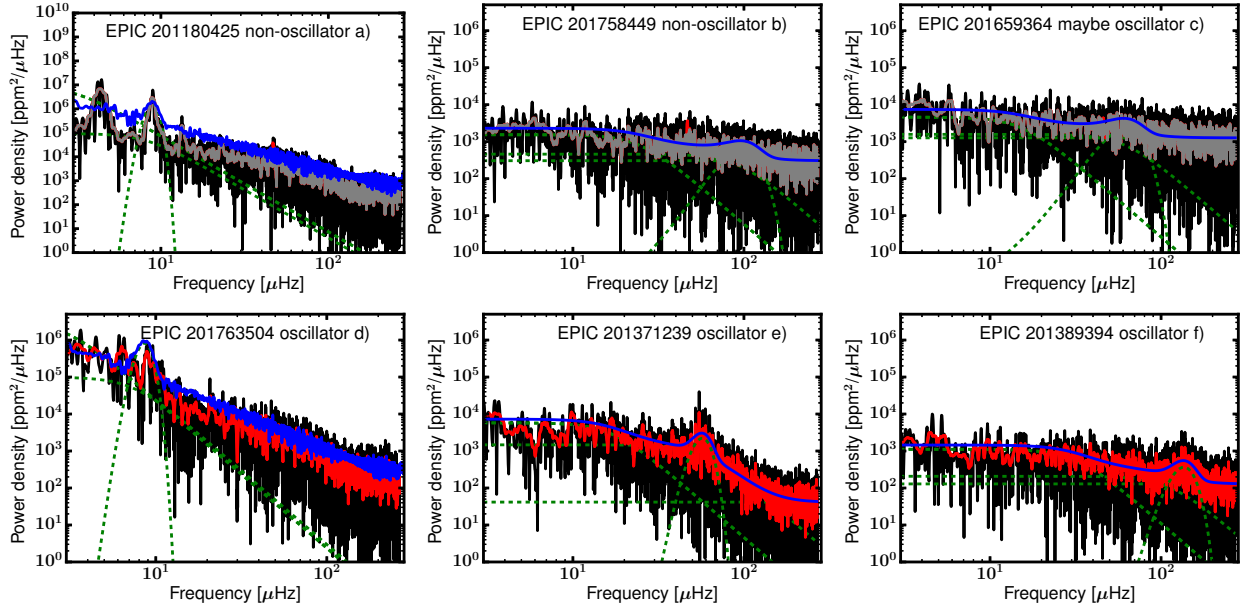


Figure 8. Examples of the raw (black) and smoothed (red) power spectra of giant candidates selected by BAM, by requiring that the WBIC favor Equation 5 over Equation 2 (see §3.6). Each component of the models is shown in green dashed curves (white noise, Gaussian excess, and Harvey components), with the total model in blue. The top row shows BAM giant candidates determined to be false positives by visual inspection: EPIC 201180425 (a) shows a periodic signal, an alias of which BAM has mistaken for solar-like oscillations; EPIC 201758449 (b) shows a dwarf-like power spectrum that is at best a borderline no/maybe case — BAM has converged on a suboptimal model in this case, in addition; and EPIC 201659364 (c) shows what may be a giant spectrum with no discernible oscillation modes. In all panels in this row, shown in grey is a smoothed VJ spectrum when the thruster firing has been removed according to the procedure described in §2. The bottom row shows BAM giant candidates confirmed by visual inspection. The model of EPIC 201763504 (d) has been convolved with the spectral window, which allows BAM to fit the correct ν_{\max} at $\sim 8\mu\text{Hz}$ rather than the spectral noise at $\sim 50\mu\text{Hz}$ (see text).

greater than 95% according to the same procedure used in Chaplin et al. (2011). However, here we assume $\sqrt{A_{\max}} = 2.5 (L/L_{\odot})^{0.9} (M/M_{\odot})^{-1.7} (T_{\text{eff}}/T_{\text{eff}, \odot})^{-2.0}$ (Stello et al. 2011) and noise equal to that of *K2*. The use of a stellar population model of C1 like this is to make population-level statements about the concordance between the observed non-GAP giant population with a simulated one, and ideally to come to conclusions regarding the completeness and purity of the BAM non-GAP giant sample. In what follows, we will argue that there are likely inadequacies in both the recovered observed distribution due to selection effects, as well as inadequacies on the modeling side due to a difficult selection function and a probable metallicity offset in *Galaxia*’s underlying stellar models.

In order to make a fair comparison between the observed non-GAP targets and the non-GAP *Galaxia* stars, we re-sampled the *Galaxia* simulation such that it reproduced the observed non-GAP distribution in $(J - K_s, H)$ space. We first binned the observed non-GAP stars in $(J - K_s, H)$ space, and assigned each bin a probability of sample membership proportional to the number of stars in that bin, and such that the sum of each bin’s probabilities summed to unity. We then

binned the *Galaxia* non-GAP stars using the same bins, and re-sampled the stars by drawing a star one-by-one with a probability equal to the aforementioned sample membership probability of the bin in which it falls. The bins were chosen to optimize agreement with the simulated and observed distributions in $(J - K_s, H)$ space, and were approximately (0.05mag, 1mag) in width. The re-sampling stopped when the number of stars with $Kp < 13$ equalled the number of stars in the observed non-GAP sample with $Kp < 13$ (2080 stars in total).⁵ This process results in some stars having the same properties because there are not enough unique *Galaxia* stars to match the number of observed stars. For this reason, we added a spread of 3% on the simulated giants’ ν_{\max} , $\Delta\nu$, and 2% on photometry to avoid a sample with identical stars. The re-sampled *Galaxia* distribution is shown in the grey contours in Figure 9. The blue contours show the observed non-GAP population that we wanted to simulate, which shows the simulation is consistent with the observations. The simulated giants

⁵ 12839 out of the 13016 non-GAP stars had valid Kp values in the EPIC, 11579 of those had valid $J - K_s$ colors, and 2080 of those also had $Kp < 13$.

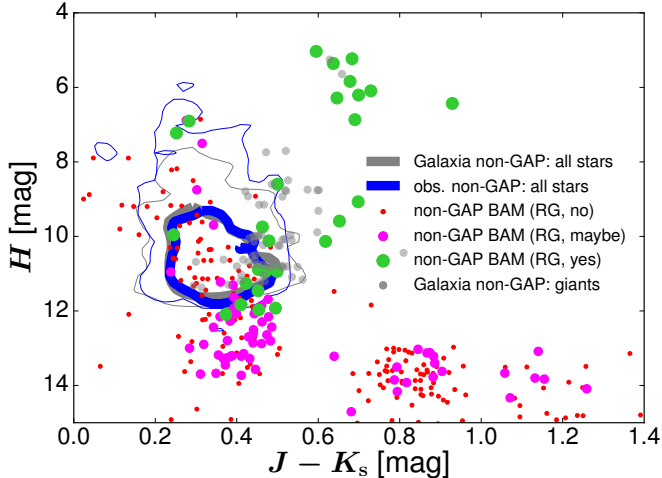


Figure 9. A color–magnitude diagram for *Galaxia* stars not passing GAP selection criteria (grey contours); *Galaxia* giants not passing GAP selection criteria, with $> 95\%$ probability of detection (grey dots); and observed non-GAP stars (blue contours). Contours enclose 68% (thick lines) and 95% (thin lines) of stars in the plotted region. Contours have been smoothed for illustrative purposes. Overlaid are stars from the non-GAP C1 target sample returned by BAM that visual inspection classified as definitely oscillators (green dots; 31 stars), maybe oscillators (magenta dots; 73 stars), and not oscillators (red dots; 212 stars).

within this sample, defined as mentioned above to have $3\mu\text{Hz} < \nu_{\text{max}} < 290\mu\text{Hz}$, $Kp < 13$, and a probability of detection greater than 95%, are shown by the grey dots.

4.3. Comparison to *Galaxia*

With the *Galaxia* model for the non-GAP giants in hand, we can proceed to evaluate the agreement between simulation and observation, with implications for both the purity/completeness of the BAM sample, as well as the fidelity of the *Galaxia* simulation in its description of the data. Figure 9 shows that the recovered giants (magenta and green dots) occupy two primary magnitude–color loci: 1) bright, red objects ($H < 7$ and $J - K_s > 0.5$), which were not targeted in GAP because of the the brightness cut in GAP of $H > 7$, and 2) giants at a typical magnitude, but bluer than typical giants ($7 < H < 13$ and $J - K_s < 0.5$), which were not in GAP because they have $J - K_s < 0.5$. First, let us consider the blue ($J - K_s < 0.5$) giants, which are the more numerous population. That *Galaxia* predicts the presence of this population (grey dots) is the best indicator of agreement between our simulations and observations. Indeed, we expect the blue population of non-GAP giants is a result of at least two factors: 1) the GAP $J - K_s > 0.5$ selection is arbitrary and there are genuine oscillators with $J - K_s < 0.5$, and 2) due to pho-

tometric errors (taken to be ~ 0.02 in the *Galaxia* C1 simulation), some oscillating giants with $J - K_s > 0.5$ will be scattered to $J - K_s < 0.5$. The *Galaxia* simulation also successfully predicts the bright ($H < 7$) giants should exist. Note that our simulations only extend to our completeness cut of $Kp = 13$, and so we do not comment on *Galaxia* agreement in the regime of $H > 12$.

If the non-GAP sample were drawn from a similar distribution as our *Galaxia* simulation, we would expect the ratio of red ($J - K_s > 0.5$) to blue ($J - K_s < 0.5$) giants in *Galaxia* to agree with that of recovered BAM giants. We take the ratio of the observed number of published ‘yes’ and ‘maybe’ oscillators from *K2* GAP DR1 (Stello et al. 2017; with $Kp < 13$ and $J - K_s > 0.5$ cuts applied) to those with $J - K_s < 0.5$ from the new, non-GAP giant sample presented here, and compare it to the expected ratio from *Galaxia*. For this test, the $(J - K_s, H)$ distribution of the GAP population was simulated in *Galaxia* following the sample membership probability procedure described above, only using the GAP targets instead of the non-GAP targets. Giants were then chosen to have $3\mu\text{Hz} < \nu_{\text{max}} < 290\mu\text{Hz}$, a probability of detection greater than 95%, and $Kp < 13$. The resulting ratio for *Galaxia* of 13 ± 2 is significantly less than the same ratio for the BAM distribution of ‘yes’ and ‘maybe’ GAP giants of 38 ± 9.0 , accounting for Poisson errors. Either the number of GAP giants are at odds with predictions, the number of non-GAP giants are, or both. Looking at the absolute numbers of giants in this ratio, 651/17 for observed BAM giants and 821/64 for *Galaxia*, the GAP giants agree better in number with what is expected from *Galaxia* than do the non-GAP giants. The 70% deficit in observed giants compared to *Galaxia* for the blue, non-GAP giants indicates that *Galaxia* predicts too many blue giants and/or BAM recovers too few blue giants. We consider both effects, in turn.

One of the primary effects that might result in an over-prediction in our *Galaxia* model’s number of non-GAP giants is an incorrect selection function. The *Galaxia* non-GAP sample as we have constructed it only reproduces the color-magnitude distribution of the many GO proposal targets that comprise the non-GAP sample. We expect this approach to globally describe the complex selection function of the sample, given that the GO proposals select objects based on color and magnitude cuts. Indeed, the non-GAP sample does describe well the observed sample (Figure 9). However, the majority of the GO proposals that comprise the non-GAP sample also use proper motion or reduced proper motion cuts to choose dwarfs. Although these cuts will be functions of color and magnitude, we cannot precisely

reproduce them in color and magnitude space. Therefore, we tested how many *Galaxia* non-GAP giants remained after applying a rather conservative (i.e., preserving more giants than dwarfs) reduced proper motion cut of $V + 5 \log_{10} \mu > 20(V - J) - 25$. (These cuts use the kinematic information that is stored as a part of a *Galaxia* simulation.) Only 11 non-GAP stars remained after this reduced proper motion cut, which indicates that the GO reduced proper motion cuts could explain the difference between the observed number of non-GAP giants (17) and that otherwise predicted by *Galaxia* (64). Another selection function could still be at work within the *Galaxia* model itself: an incorrect metallicity distribution of disk stars could result in too many blue giants, whose colors naturally depend on metallicity. A metallicity effect could also explain the offset in red clump position with respect to the observed red clump in *K2* data, which is discussed in the next section.

With the reduced proper motion cut’s role in mind, we still anticipate that some of the deficit in observed numbers of non-GAP giants is likely to reflect genuine incompleteness in the BAM giant sample. For example, in a handful of cases in the false positive (‘no’s) sample, BAM performed a poor fit to the data, which will mean its Bayesian model comparison will not be valid. Also, blended light from dwarfs would also strongly select against recovery with BAM because of a dilution of the oscillation signal resulting in significant departures from the amplitudes imposed by BAM’s priors in Table 1. We note also that asteroseismic giant detection with *K2* will miss giants with $\nu_{\max} \lesssim 3\mu\text{Hz}$ and $\nu_{\max} > 283\mu\text{Hz}$ — the most evolved giants, and those closest to the base of the red giant branch. Establishing robust completeness and efficiency estimates is not the purpose of this paper, however, and we will explore these concerns more thoroughly in the next K2GAP data release (Zinn et al., in prep.).

We can also compare the *Galaxia* non-GAP red giant sample and the observed BAM non-GAP red giant sample in magnitude- ν_{\max} space, as shown in Figure 10. Kolmogorov-Smirnov tests indicate that both the ν_{\max} distribution and Kp distribution for the definite BAM red giants are in $\sim 3.2\sigma$ and $\sim 4.0\sigma$ tension with the *Galaxia* ν_{\max} and Kp distributions, assuming our adopted detection limit of $Kp < 13$. We note at this point that the procedure to match observed and *Galaxia* magnitude and color distributions (§4.2) is stochastic because the distributions are matched by drawing from probability distributions. This results in the *Galaxia* giants having ν_{\max} and Kp distributions that vary in their agreement with the observed non-GAP giant distributions, fluctuating at the 0.3σ and

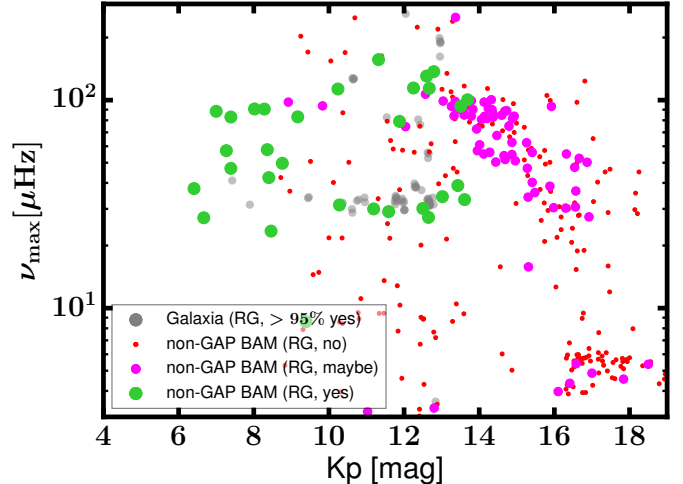


Figure 10. ν_{\max} - Kp distribution of *Galaxia* predicted detections of non-GAP oscillating giants (grey). Overlaid are stars from the non-GAP C1 target sample returned by BAM that visual inspection classified as definitely oscillators (green dots; 31 stars), maybe oscillators (magenta dots; 73 stars), and not oscillators (red dots; 212 stars).

0.4σ level, respectively. Keeping this caveat in mind, there is still a tension in the simulated and observed ν_{\max} distributions when marginalizing over realizations of the *Galaxia* ν_{\max} distribution. That the tension in ν_{\max} space decreases by $\sim 1\sigma$ with a reduced proper motion cut (see §4.2), indicates this difference might be due to the un-modelled non-GAP selection function effects of individual GO proposals. There could also certainly be a ν_{\max} -dependent efficiency in BAM identifying giants. Indeed, the latter effect is seen across various pipelines when comparing to a ground truth set of giants in *K2* fields identified by eye, even while *Galaxia* giant predictions as a function of ν_{\max} agree very well with the ground truth (K2GAP DR2; Zinn et al., in prep.).

4.4. Properties of *Galaxia* and observed non-GAP giants

We show in Figures 11 and 12 the $\Delta\nu$ - ν_{\max} and A_{\max} - ν_{\max} relations for this sample (colored points), as well as for the *Galaxia* model (black points). We have also included BAM GAP giants published in Stello et al. (2017), for reference (grey points). The agreement between model and observed properties in these spaces is good, except for the clump, for which *Galaxia* predicts a too-high $\Delta\nu$ and A_{\max} . We can see that *Galaxia* over-predicts $\Delta\nu$ and A_{\max} (and does not under-predict ν_{\max}) because the ν_{\max} location of the over-density in GAP BAM stars at $\nu_{\max} \sim 30\mu\text{Hz}$ agrees with the location of the over-density in the non-GAP *Galaxia* stars. Figure 13 shows a modified Kiel diagram, in which $J - K_s$

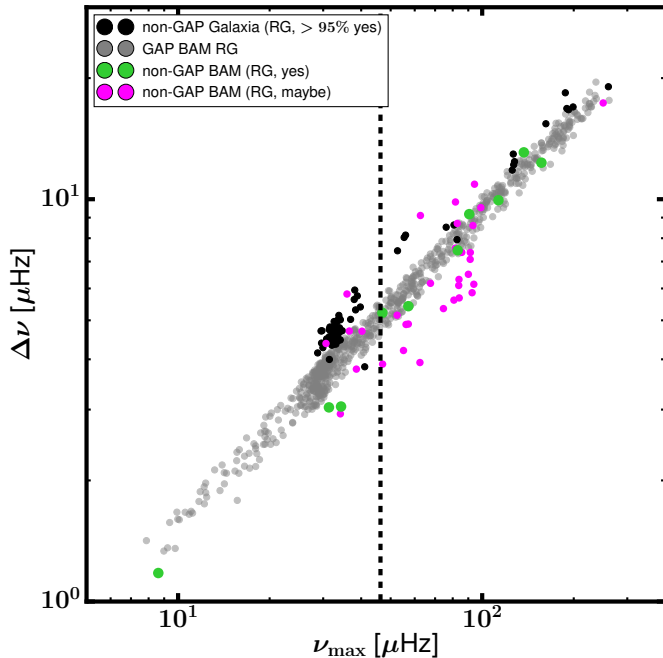


Figure 11. The $\Delta\nu$ - ν_{\max} relation, with the non-GAP giant sample shown as points with colors as in Figure 10, comprising stars that have both $\Delta\nu$ and ν_{\max} measured by BAM. Grey points are BAM results from K2GAP DR1 (Stello et al. 2017), and black points are from our *Galaxia* simulation of the non-GAP giant sample. The dashed line corresponds to the nominal *K2* thruster firing frequency.

color is used instead of temperature and ν_{\max} instead of gravity⁶. In this space, we can see that nearly all of the observed non-GAP sample is found at or below the clump (at $\nu_{\max} \sim 30\mu\text{Hz}$), and that the location of the *Galaxia* clump overlaps with several of the presumable observed red clump stars, confirming that the *Galaxia* clump ν_{\max} locus is not discrepant with the observed locus. That the modeled clump $\Delta\nu$ locus is offset from the observed clump $\Delta\nu$ locus is another indication that the *Galaxia* models could be relying on a Galactic metallicity distribution at odds with the actual one — a conclusion that one arrives at when comparing *Galaxia* stellar parameters to those from asteroseismology in other *K2* campaigns (Sharma et al. 2019).

4.5. Implications for dwarf selection purity

A summary of the number of ‘yes’ and ‘maybe’ giants broken down by the GO target list from which they arise is shown in Table 4. 21 of the sample of non-GAP giants are serendipitous: they are only targets from GO proposals that do not intentionally select giants. This, in

⁶ Note the reversed y-axis: a smaller ν_{\max} means a smaller gravity, and so is in the sense of a normal Kiel diagram.

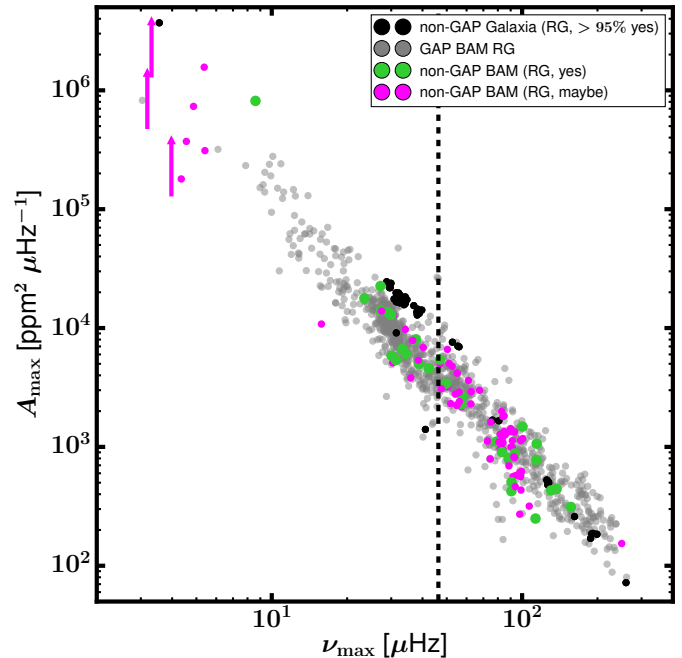


Figure 12. The A_{\max} - ν_{\max} relation, with the non-GAP giant sample shown as points with colors as in Figure 10. Giants for which $\nu_{\max} \lesssim 4\mu\text{Hz}$ are considered upper limits. Grey points are BAM results from K2GAP DR1 (Stello et al. 2017), and black points are from our *Galaxia* simulation of the non-GAP giant sample. BAM K2GAP DR1 amplitudes were not published in (Stello et al. 2017), though are reproduced here. The dashed line corresponds to the nominal *K2* thruster firing frequency.

turn, allows us to say that the purity of giant exclusion across *K2* C1 GO proposals is $\sim 99\%$, based on the observed confirmed number of serendipitous giants found among the GO target lists that do not purport to select giants (those that intentionally target giants are not included in our calculation of dwarf purity, and are noted in Table 4). The purity decreases a negligible amount if also including the BAM non-GAP ‘maybe’ giants. This estimated dwarf selection purity is an upper bound because we have certainly not recovered all the giants due to reasons discussed in §4.2. In this estimate, we have only counted targets that are within our completeness limit of $Kp < 13$. In this sense, we confirm that the *K2* dwarf samples chosen with color and proper motion cuts are generally free from giants for $Kp < 13$.

5. CONCLUSION

In this paper, we have presented the BAM pipeline, which calculates global oscillation parameters in a Bayesian framework. A major advantage of the Bayesian fitting method we have employed is its natural basis for probabilistic selection of likely true oscillators among

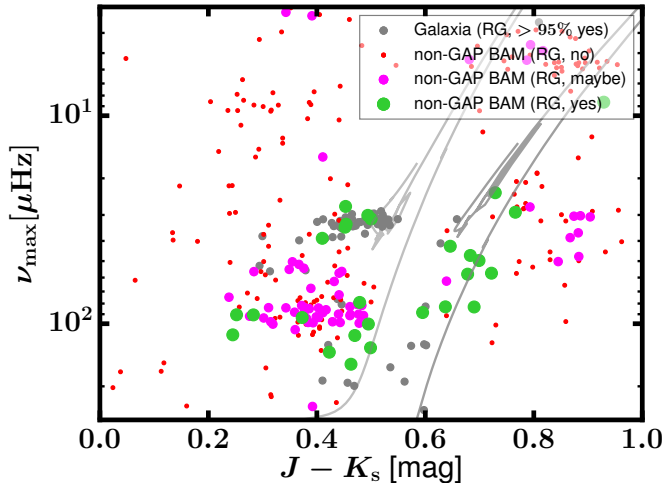


Figure 13. Modified Kiel diagram, with the non-GAP giant sample shown as points with colors as in Figure 10. The grey points are predictions from a simulation of the non-GAP stellar population in Campaign 1 using *Galaxia* (Sharma et al. 2011). See text for details. Evolutionary tracks for a $1.3M_{\odot}$ star with $[\text{Fe}/\text{H}] = 0$ (dark grey) and $[\text{Fe}/\text{H}] = -1$ (light grey) from MIST (Dotter 2016; Choi et al. 2016) are shown for visualization purposes.

a collection of light curves. In the process of developing this pipeline and applying it to *K2* Campaign 1 (C1) stars, including both Galactic Archaeology Program (GAP; Stello et al. 2015, 2017) giant targets and non-GAP dwarf targets, we have found the following:

1. We have identified as-of-yet an unidentified noise pattern present in Vanderburg & Johnson (2014) light curves of C1 stars that causes a splitting of the nominal thruster firing frequency artefact at $47.22\mu\text{Hz}$ in a time-dependent manner.
2. We have additionally shown that it is necessary to account for the spectral window in fitting the spectra of solar-like oscillators in order to model the unphysical spectral leakage in the power spectrum of oscillators with $\nu_{\text{max}} \lesssim 15 \mu\text{Hz}$. In this work, we have done so by convolving models of the granulation with the observed window function.
3. We have benchmarked our asteroseismic parameters against the existing SYD asteroseismic pipeline, and quantified statistical and systematic errors for BAM parameters accordingly. We find typical errors for *K2* BAM giants in ν_{max} and $\Delta\nu$ of $\sim 1.53\%(\text{random}) \pm 0.2\%(\text{systematic})$ and $1.51\%(\text{random}) \pm 0.6\%(\text{systematic})$.
4. As an example application of BAM, we have also presented a sample of 104 non-GAP BAM red gi-

ants and red giant candidates from C1 identified by their solar-like oscillations, 91 of which were not selected by Guest Observer proposals to be giants, and hence are serendipitous discoveries.

5. The size of the non-GAP BAM red giant sample suggests that *K2* C1 dwarf samples chosen with color and proper motion cuts are generally free from giants for $Kp < 13$ to a high degree (upper bound of $\sim 99\%$ pure).
6. Simulated *Galaxia* C1 non-GAP giant populations are in tension with the Kp and ν_{max} distributions of observed non-GAP giants with $Kp < 13$ found by BAM. When considering also the higher-than-observed number of blue ($J - K_s < 0.5$) giants in the *Galaxia* model, the disagreement between model and observation can be explained by the proper motion cuts used to select the non-GAP targets. There is also likely incompleteness in the BAM giant detection process, which will be addressed in future work. Finally, the *Galaxia* metallicity distribution is likely different than the distribution of the non-GAP stars (Sharma et al. 2019).

BAM promises to robustly identify and characterize solar-like oscillators in *K2* and the TESS mission (Ricker et al. 2014), which is observing hundreds of thousands of red giants with at least 30 minute cadence. Though it will perform at least as well as *K2* in resolving oscillations on the lower giant branch, the majority of TESS’s red giant data will have roughly half the temporal baseline of *K2*, and therefore will be a factor of two worse in spectral resolution. Spectral resolution is particularly important in identifying the low frequency oscillators like those presented here. In this sense, BAM’s Bayesian fitting techniques will take advantage of the information in (‘global’) features of the power spectrum that are less sensitive to degraded frequency resolution, in order to robustly identify ν_{max} for TESS giants.

We thank the referee for their comments, which improved both BAM and the contents of this paper. J. Z. acknowledges support from NASA grants 80NSSC18K0391 and NNX17AJ40G. D. H. acknowledges support by the National Science Foundation (AST-1717000) and the National Aeronautics and Space Administration under Grants NNX14AB92G and NNX16AH45G issued through the *Kepler* Participating Scientist Program and the *K2* Guest Observer Program. D. S. is the recipient of an Australian Research Council Future Fellowship (project number FT1400147). Parts

of this research were conducted by the Australian Research Council Centre of Excellence for All Sky Astrophysics in 3 Dimensions (ASTRO 3D), through project number CE170100013. This research was supported in part by the National Science Foundation under Grant No. NSF PHY-1748958 and by the Heising-Simons Foundation.

This paper includes data collected by the *K2* mission. We thank all NASA employees that have contributed to the remarkable success of the *K2* mission. Funding for the *K2* mission is provided by the NASA Science Mission directorate. Some of the data presented in this paper were obtained from the Mikulski Archive for Space Telescopes (MAST).

Table 3. Campaign I non-GAP BAM asteroseismic parameters for giants and giant candidates

EPIC	2MASS	RA	Dec	ν_{\max}	ν_{\max}	$\sigma_{\nu_{\max}}$	$\Delta\nu$	$\sigma_{\Delta\nu}$	A_{\max}	$\sigma_{A_{\max}}$	σ_{meso}	σ_{meso}	σ_{meso}	τ_{gran}	$\sigma_{\tau_{\text{gran}}}$	WN	σ_{WN}	giant? ^a		
		deg	deg	μHz	μHz	μHz	μHz	μHz	$\text{ppm}^2 \mu\text{Hz}^{-1}$	$\text{ppm}^2 \mu\text{Hz}^{-1}$	ppm	ppm	μHz^{-1}	μHz^{-1}	μHz^{-1}	$\text{ppm}^2 \mu\text{Hz}^{-1}$	μHz^{-1}	$\text{ppm}^2 \mu\text{Hz}^{-1}$		
201147434	11452628-0521209	176.359512	-5.355842	67.604	2.676	6.179	0.696	2.994e+03	9.890e+02	4.081e+02	4.279e+01	1.977e-02	1.790e-03	4.936e+02	3.934e+01	4.681e-03	4.733e-04	1.125e+03	1.211e+01	1
201151637	11360854-0511520	174.035575	-5.256981	57.160	4.415	4.894	0.021	2.166e+03	1.287e+03	4.491e+02	3.038e+01	2.230e-02	3.120e-03	5.273e+02	2.435e+01	5.841e-03	3.477e-04	5.719e+02	1.328e+01	1
201156121	11315343-0408579	172.972654	-5.149433	51.849	3.264	2.314e+03	1.125e+03	3.754e+02	3.378e+01	2.725e-02	4.432e-03	4.530e+01	2.530e+01	6.410e-03	5.875e-04	1.159e+03	2.892e+01	1
201163464	11353033-0405826	173.876408	-4.973911	52.509	3.362	5.149	0.018	4.768e+03	3.751e+03	5.603e+02	4.441e+01	2.319e-02	3.10e-03	6.850e+02	3.972e+01	5.976e-03	4.948e-04	2.425e+03	5.196e+01	1
201198517	11391931-0408141	174.830492	-4.137267	42.417	6.645	4.554e+03	6.148e+03	1.235e+02	5.464e+01	3.896e-02	2.187e-03	5.012e+02	1.577e+01	3.189e-04	6.436e+01	5.346e+00	2	
201214537	11461882-0345352	176.578525	-3.759797	51.098	4.421	5.040e+03	3.956e+03	5.377e+02	3.964e+01	2.843e-02	3.819e-03	7.327e+02	3.243e+01	5.561e-03	3.705e-04	2.272e+03	4.871e+01	1
201228292	1131589-0332138	171.216150	-3.537211	50.382	2.234	3.211e+03	2.136e+03	4.665e+02	3.551e+01	2.524e-02	3.378e-03	5.765e+02	2.944e+01	5.763e-03	4.952e-04	1.290e+03	3.113e+01	1
201244712	11233476-0317127	170.894883	-3.289417	49.686	0.704	3.406e+03	6.118e+02	8.720e+02	3.486e+01	2.863e-02	1.788e-03	6.132e+02	2.231e+01	6.004e-03	1.920e-04	8.177e+01	2.313e+00	2
201251246	11291517-0311199	172.313354	-3.188886	3.309	2.566e+06	8.814e+05	4.222e+02	3.550e+02	3.516e-01	3.131e-02	3.295e+03	2.028e+02	8.672e-02	6.170e-03	6.972e+01	4.575e+00	2
201253257	...	179.712362	-3.158483	55.077	4.786	4.172e+03	3.050e+03	4.662e+02	4.151e+01	2.424e-02	3.321e-03	7.106e+02	3.180e+01	5.625e-03	3.720e-04	1.646e+03	3.615e+01	1
201262747	11542756-0300552	178.614854	-3.015358	98.614	4.590	5.610e+02	2.737e+02	3.355e+02	1.901e+01	1.305e-02	1.457e-03	3.358e+02	1.925e+01	3.774e-03	3.295e-04	3.586e+02	8.709e+00	1
201269306	11235529-0254559	170.980417	-2.915544	114.376	0.673	1.065e+03	9.483e+01	4.929e+02	1.667e+01	1.176e-02	6.325e-04	3.587e+02	1.476e+01	3.408e-03	1.805e-04	8.608e+01	2.869e+00	2
201272934	11190372-0251388	169.765562	-2.860719	89.965	7.486	1.427e+03	9.458e+02	4.507e+02	3.229e+01	1.387e-02	1.517e-03	5.431e+02	3.221e+01	3.682e-03	3.046e-04	1.025e+03	2.614e+01	1
201305005	11374947-0222333	174.456163	-2.375928	30.647	2.360	4.379	0.058	1.281e+04	9.055e+03	1.019e+03	7.423e+01	4.373e-02	3.892e-03	8.133e+02	6.819e+01	9.908e-03	9.029e-04	6.525e+03	1.110e+02	1
201310650	11351161-0217353	173.798379	-2.293164	47.040	4.038	3.891	0.022	5.000e+03	3.903e+03	5.739e+02	4.526e+01	2.915e-02	3.419e-03	7.150e+02	3.875e+01	6.180e-03	5.059e-04	2.635e+02	5.599e+01	1
201348966	11305689-0143174	172.737462	-1.721542	38.852	1.057	4.974e+03	1.102e+03	5.837e+02	3.973e+01	3.047e-02	2.635e-03	7.066e+02	2.502e+01	7.802e-03	2.314e-04	1.159e+02	2.597e+00	2
201361246	12005920-0132144	180.246675	-1.537347	47.547	5.332	3.093e+03	2.187e+03	5.869e+02	4.346e+01	2.613e-02	4.348e-03	6.068e+02	3.927e+01	7.203e-03	7.921e-04	1.866e+03	4.179e+01	1
201361404	11112565-0132069	167.856942	-1.535272	100.372	0.903	1.482e+03	3.635e+02	4.316e+02	2.491e+01	1.144e-02	1.093e-03	4.287e+02	2.480e+01	3.316e-03	2.431e-04	3.794e+02	1.135e+01	2
201370145	11130872-0124345	168.286287	-1.409614	82.959	1.019	1.266e+03	1.318e+02	5.517e+02	1.280e+01	1.510e-02	8.499e-04	4.355e+02	1.811e+01	4.215e-03	1.461e-04	4.157e+01	1.464e+00	2
201371239	11111931-0123405	167.830442	-1.394597	57.161	0.813	5.421	0.018	2.287e+03	3.498e+02	5.523e+02	2.636e+01	1.894e-02	1.235e-03	5.211e+02	2.139e+01	5.413e-03	1.759e-04	4.157e+01	1.183e+00	2
201374034	11062714-0121136	166.613092	-1.353819	98.965	6.816	9.528	0.028	4.333e+02	2.267e+02	2.891e+02	1.616e+01	1.252e-02	1.068e-03	2.729e+02	1.612e+01	3.694e-03	3.402e-04	2.290e+02	5.639e+00	1
201375598	11194625-0119486	169.942750	-1.330181	4.559	0.941	0.731	0.016	3.717e+05	3.404e+05	2.476e+02	5.092e+02	2.255e-01	5.046e-02	2.637e+02	1.876e+02	7.317e-02	1.505e-02	8.340e+04	1.384e+03	1
201379262	11234526-0116277	170.940087	-1.274369	40.242	5.022	4.699	0.051	6.862e+03	5.470e+03	6.450e+02	5.438e+01	3.529e-02	5.422e-03	8.063e+02	4.876e+02	7.269e-03	8.057e-04	4.611e+04	9.516e+01	1
201379481	...	168.657175	-1.270828	37.570	0.758	8.026e+03	1.018e+03	1.091e+03	4.372e+01	3.813e-02	2.345e-03	5.955e+02	3.462e+01	5.662e-03	2.493e-04	3.954e+01	3.093e+00	2
201389394	11082147-0107156	167.089500	-1.121086	137.060	1.990	13.075	0.049	4.433e+02	5.241e+01	3.329e+02	1.265e+01	1.006e-02	5.729e-04	2.704e+02	1.439e+01	2.838e-03	2.119e-04	1.289e+02	4.161e+00	2
201400095	11210314-0057399	170.263029	-0.961072	50.276	4.850	6.613e+03	3.500e+03	6.171e+02	4.821e+01	5.35e-02	2.918e-03	7.800e+02	4.464e+01	6.060e-03	5.457e-04	3.689e+03	7.561e+01	1
201411387	11232145-0047048	170.839412	-0.784719	38.573	3.427	3.782	0.032	5.361e+03	3.500e+03	7.352e+02	5.184e+01	3.525e-02	3.285e-03	2.886e+02	4.463e+01	7.732e-03	6.768e-04	3.371e+03	6.706e+01	1
201414774	11252575-0044016	171.357304	-0.733783	4.869	0.363	7.325e+05	3.186e+05	2.949e+03	5.548e+02	2.350e-01	2.549e-02	3.273e+02	2.135e+02	6.460e-02	4.725e-03	2.207e+04	4.225e+02	1
201415775	11333341-0043060	173.389225	-0.718339	27.298	0.294	1.405e+04	2.691e+03	9.926e+02	7.152e+01	4.837e-02	2.932e-03	5.915e+02	3.877e+01	9.928e-03	4.971e-04	3.234e+01	2.713e+00	2
201428887	11361104-00222409	174.046021	-0.378047	33.244	0.805	6.643e+03	1.246e+03	6.136e+02	4.458e+01	3.751e-02	3.055e-03	7.234e+02	2.309e+01	7.648e-03	2.576e-04	1.427e+02	3.323e+00	2
201454791	11453665-0009037	176.402708	-0.151056	130.534	1.069	4.305e+02	3.249e+01	3.025e+02	1.218e+01	9.235e-03	5.605e-04	2.150e+02	1.463e+01	2.895e-03	2.704e-04	3.790e+01	1.434e+00	2
201459357	11255698-0005024	171.487429	-0.084022	3.972	2.560e+05	2.209e+05	2.694e+02	8.544e+00	1.67e-02	4.811e-04	1.898e+02	1.666e+02	8.400e-02	8.039e-03	1.014e+04	1.748e+02	1
201467358	11422234+0002007	175.593208	0.033297	113.094	0.658	9.942	0.032	2.104e+01	2.561e+03	9.782e+02	7.404e+01	3.403e-02	2.911e-03	9.752e+02	5.070e+01	1.020e-02	4.305e-04	3.790e+01	4.029e-01	2
201472519	11441126+0006347	176.046942	0.109667	29.995	0.735	1.290e+04	1.452e+05	2.163e+03	3.068e+02	2.004e-01	3.316e-02	2.238e+02	1.779e+02	6.368e-02	6.244e-03	1.052e+04	1.785e+02	2
201508254	11110893+0038392	167.787258	0.644258	88.027	7.028	7.613e+02	5.025e+02	3.710e+02	2.034e+01	1.372e-02	1.205e-03	3.613e+02	1.763e+01	4.171e-03	3.231e-04	2.669e+02	6.714e+02	1
201508599	11260798+0039130	171.533283	0.653625	34.168	4.443	2.927	0.029	9.747e+03	9.512e+03	7.774e+02	5.589e+01	3.514e-02	3.750e-03	7.343e+02	4.661e+01	8.281e-03	8.927e-04	3.624e+03	5.932e+01	1
201512825	11432842+0043107	175.868425	0.719658	79.011	0.804	1.109e+03	9.800e+01	3.580e+02	1.692e+01	1.495e-02	1.033e-03	3.385e+02	1.569e+01	4.117e-03	1.831e-04	3.418e+01	1.180e+00	2
201515047	11504834+0045163	177.701492	0.754572	249.915	5.820	17.348	0.006	1.538e+02	1.885e+01	2.526e+02	8.249e+00	7.260e-03	4.611e-04	2.237e+02	8.993e+00	1.442e-04	6.159e+01	4.456e-01	2	
201525065	11460722+0054340	176.280079	0.909461	23.455	5.107	1.784e+04	2.212e+03	1.727e+02	6.506e+01	3.146e-02	2.692e-03	5.076e+02	3.357e+01	1.706e-02	1.278e-03	1.775e+01	4.862e+00	2
201526688	11461610+0056057	176.567104	0.934933	36.565	4.112	4.703	0.047	7.871e+03	6.151e+03	7.356e+02	6.506e+01	3.705e-02	4.139e-03	5.143e+02	5.311e+01	8.109e-03	6.968e-04	4.172e+03	8.413e+01	1
201555742	11272268+0122258	171.844575	1.373844	46.977	0.559	5.220	0.010	5.428e+03	6.818e+02	7.309e+02	3.682e+01	2.409e-02	2.847e-03	6.774e+02	2.712e+01	5.407e-03	2.915e-04	7.148e+01	2.407e+00	2
201584221	11012278+0147570	167.594996	1.799169	54.805	2.963	2.233e+03	1.476e+03	4.817e+02	2.958e+01	2.349e-02	2.103e-03	5.422e+02	2.418e+01	5.407e-03	3.761e-04	1.134e+03	2.482e+01	1
201601287	11151790+0203483	168.824604	2.063439	57.788	0.667	2.676e+03	4.368e+02	4										

Table 3 (continued)

EPIC	2MASS	RA	Dec	ν_{\max}	$\sigma_{\nu_{\max}}$	$\Delta\nu$	$\sigma_{\Delta\nu}$	A_{\max}	$\sigma_{A_{\max}}$	σ_{meso}	σ_{meso}	τ_{meso}	$\sigma_{\tau_{\text{meso}}}$	σ_{gran}	σ_{gran}	τ_{gran}	$\sigma_{\tau_{\text{gran}}}$	WN	σ_{WN}	giant?*
		deg	deg	μHz	μHz	μHz	μHz	$\text{ppm}^2 \mu\text{Hz}^{-1}$	$\text{ppm}^2 \mu\text{Hz}^{-1}$	ppm	ppm	μHz^{-1}	μHz^{-1}	ppm	ppm	μHz^{-1}	μHz^{-1}	$\text{ppm}^2 \mu\text{Hz}^{-1}$	$\text{ppm}^2 \mu\text{Hz}^{-1}$	
201619206	11204791+0220248	170.199588	2.340211	30.413	2.190	5.101e+03	3.665e+03	7.108e+02	5.437e+01	4.403e-02	5.538e-03	5.629e+02	4.172e+01	9.954e-03	8.876e-04	2.377e+03	4.599e+01	1
201620616	12012949+0221443	180.372892	2.362361	97.836	1.976	2.716e+02	4.170e+01	2.263e+02	1.223e+01	1.206e-02	9.010e-04	2.105e+02	1.176e+01	3.834e-03	2.662e-04	7.108e+01	1.758e+00	1
201629903	12000308+0229322	180.012879	2.492258	91.308	4.808	7.088	0.014	9.854e+02	3.294e+02	3.062e+02	2.563e+01	1.374e-02	1.447e-03	3.960e+02	2.100e+01	4.074e-03	3.098e-04	4.810e+02	1.133e+01	1
201635902	11164254+0235580	169.176033	2.599492	56.061	3.460	2.892e+02	1.311e+03	4.498e+02	3.385e+01	2.604e-02	3.015e-03	4.963e+02	2.866e+01	5.784e-03	4.880e-04	1.286e+03	2.702e+01	1
201636027	11335625+0236055	173.484437	2.601469	3.183	9.458e+05	2.102e+05	2.693e+02	2.718e+02	3.542e-01	3.987e-02	3.608e+02	3.168e+01	1.128e-01	8.169e-03	4.455e+00	1.197e+00	1
201643723	11215719+0243098	170.488400	2.719483	35.924	3.088	5.813	0.460	3.812e+03	3.107e+03	6.480e+02	4.616e+01	3.839e-02	3.996e-03	6.961e+02	3.003e+01	7.896e-03	5.978e-04	1.973e+03	3.963e+01	1
201659364	11162508+0230136	169.104496	2.964933	62.417	4.133	3.927	0.022	2.301e+03	1.301e+03	4.730e+02	3.324e+01	2.055e-02	2.340e-03	5.534e+02	2.206e+01	5.147e-03	3.930e-04	1.266e+03	2.928e+01	1
201667626	11241443+0306133	171.060271	3.103350	30.137	1.307	5.854e+03	1.984e+03	6.626e+02	5.740e+01	3.759e-02	3.099e-03	8.035e+02	3.007e+01	9.093e-03	2.954e-04	5.443e+00	1.259e+00	2
201680913	12014373+0319161	180.432225	3.321144	55.107	2.315	4.207	0.013	2.271e+03	1.026e+03	3.333e+02	2.600e+01	2.490e-02	3.454e-03	4.304e+02	2.612e+01	5.496e-03	4.999e-04	1.001e+03	2.359e+00	1
201696051	12044299+0334230	181.179146	3.573111	88.357	3.333	8.036e+02	1.932e+02	4.894e+02	2.670e+01	1.251e-02	8.702e-04	4.415e+02	2.593e+01	4.323e-03	2.850e-04	1.950e+02	5.450e+00	2
201697539	11482814+0335534	177.117221	3.598100	15.789	0.769	1.080e+04	5.597e+03	1.201e+02	5.976e+02	8.025e-02	6.970e-03	6.937e+01	1.973e+02	1.773e-03	2.106e+03	3.720e+01	1	
201700607	11282997+0338594	172.124917	3.649897	81.719	5.318	7.558	0.052	9.614e+02	4.903e+02	3.906e+02	2.278e+01	1.605e-02	1.690e-03	8.830e+02	2.185e+01	4.127e-03	3.552e-04	5.028e+02	1.144e+01	1
201702907	...	178.026996	3.688792	74.988	7.398	1.618e+03	1.135e+03	4.119e+02	3.300e+01	1.480e-02	1.662e-03	5.439e+02	2.490e+01	4.621e-03	2.693e-04	5.542e+02	1.208e+01	1
201704568	11261591+0342583	171.566321	3.716222	97.876	2.453	6.111e+02	1.180e+02	2.721e+02	1.385e+01	1.457e-02	1.240e-03	2.750e+02	1.497e+01	3.569e-03	2.790e-04	2.393e+02	5.845e+00	1
201713224	11264919+0351517	171.704958	3.864342	31.338	0.406	3.038	0.002	5.379e+03	9.801e+02	4.816e+02	3.372e+01	3.413e-02	3.187e-03	5.307e+02	2.088e+01	9.077e-03	3.144e-04	1.661e+01	4.746e+01	2
201720476	11143920+0359154	168.663354	3.987589	83.725	7.192	6.103	0.722	1.801e+02	1.140e+03	5.019e+02	4.172e+01	1.395e-02	1.486e-03	5.545e+02	3.616e+01	4.061e-03	3.630e-04	1.023e+03	2.439e+01	1
201722766	11240739+0401380	171.030762	4.027258	88.538	4.371	6.930e+02	2.708e+02	3.104e+02	1.907e+01	1.441e-02	1.370e-03	3.437e+02	1.855e+01	3.847e-03	3.201e-04	3.768e+02	9.177e+00	1
201724514	11582220+0403262	179.592525	4.057289	29.111	0.611	1.355e+04	2.703e+02	1.070e+03	7.104e+01	3.660e-02	2.477e-03	3.958e+02	4.733e+01	6.189e-02	6.429e-03	1.901e+01	2.827e+03	1
201724852	11162791+0403471	168.116350	4.063117	94.344	6.219	10.897	0.046	5.750e+02	2.997e+02	3.066e+02	1.903e+01	1.342e-02	1.369e-03	3.039e+02	1.823e+01	3.961e-03	3.720e-04	3.552e+02	8.529e+00	2
201726163	11150267+0405078	168.761167	4.085508	93.244	2.575	8.602	0.038	1.338e+03	3.435e+02	3.942e+02	3.385e+01	1.153e-02	1.159e-03	5.179e+02	2.848e+01	4.104e-03	2.688e-04	5.624e+02	1.442e+01	1
201729267	11230257+0408173	170.760737	4.138147	92.008	2.000	5.634e+02	1.083e+02	2.784e+02	1.703e+01	1.185e-02	8.909e-04	3.272e+02	1.356e+01	3.366e-03	1.919e-04	1.166e+02	3.677e+00	1
201733406	11213386+0412299	170.391112	4.208306	90.679	1.445	9.181	1.372	5.055e+02	7.600e+01	2.350e+02	2.280e+01	1.409e-02	1.177e-03	2.298e+02	1.339e+01	3.770e-03	3.325e-04	1.147e+02	3.052e+00	2
201743103	11170064+0421565	169.252658	4.365717	84.644	5.676	1.348e+03	6.447e+02	4.056e+02	2.541e+01	1.562e-02	1.488e-03	4.229e+02	2.519e+01	4.144e-03	3.056e-04	6.171e+02	1.591e+01	1
201747404	11390558+0426188	174.773221	4.438600	156.608	1.034	12.324	0.674	3.123e+02	2.315e+01	2.616e+02	8.140e+00	9.993e-03	6.149e-04	2.087e+02	8.171e+02	2.669e-03	1.708e-04	3.179e+01	1.310e+00	2
201749662	11153895+0428104	168.912304	4.477769	90.375	1.455	4.239e+02	5.398e+01	2.96e+02	1.100e+01	1.732e-02	1.438e-03	1.801e+02	1.138e+01	3.903e-03	3.090e-04	9.589e+01	2.272e+00	2
201750985	11292465+0429584	172.352729	4.499581	27.465	0.976	1.380e+03	4.681e+03	9.214e+02	7.938e+01	4.705e-02	4.102e-03	7.151e+02	1.105e+01	1.146e-02	1.011e-03	5.044e+03	9.507e+01	1
201751998	11160874+0431029	169.036404	4.517472	54.093	1.772	2.776e+03	1.131e+03	3.731e+02	2.817e+01	2.365e-02	2.788e-03	5.354e+02	2.422e+01	5.059e-03	3.211e-04	5.837e+02	1.943e+01	1
201752633	11121723+0431442	168.071796	4.528894	106.785	6.842	3.175e+02	1.511e+02	3.065e+02	1.540e+01	1.126e-02	9.700e-04	3.141e+02	1.352e+01	3.527e-03	2.658e-04	1.077e+02	3.486e+00	1
201758449	11175773+0437487	169.490575	4.630186	99.409	5.084	6.210e+02	2.615e+02	4.69e+02	1.888e+01	1.279e-02	1.011e-03	3.648e+02	1.932e+01	3.452e-03	2.673e-04	3.053e+02	8.457e+00	1
201768504	11152022+0441023	168.834287	4.683992	88.898	3.367	1.347e+03	5.248e+02	4.625e+02	2.959e+01	1.286e-02	1.096e-03	4.554e+02	2.774e+01	4.162e-03	3.229e-04	7.687e+02	6.284e+00	1
201768504	1148335+0443022	177.138908	4.717314	8.609	0.139	1.177	0.158	8.146e+05	1.573e+05	5.359e+03	3.332e+02	1.075e-01	6.684e-03	1.519e+03	2.472e+02	4.300e-02	3.608e-03	3.880e-01	9.678e-01	2
201765667	11145908+0445177	168.746204	4.754925	85.684	4.221	7.375	0.050	1.266e+03	4.148e+02	3.232e+02	2.353e+01	1.742e-02	1.930e-03	4.094e+02	2.394e+01	4.006e-03	3.893e-04	6.068e+02	1.375e+01	1
201766812	11150311+0446301	168.762396	4.775025	100.462	4.872	1.175e+03	4.130e+02	4.083e+02	2.828e+01	1.300e-02	1.230e-03	4.734e+02	2.518e+01	3.561e-03	3.001e-04	5.436e+02	1.521e+01	1
201772439	1112479+0452234	167.853371	4.873231	98.648	2.035	1.127e+03	2.578e+02	4.209e+02	2.540e+01	1.434e-02	1.340e-03	4.923e+02	1.984e+01	3.732e-03	2.733e-04	3.643e+02	1.059e+01	1
201774359	11162408+0454236	169.100333	4.906556	72.644	5.287	1.120e+03	5.598e+02	3.210e+02	1.958e+01	1.865e-02	1.844e-03	3.651e+02	1.782e+01	4.662e-03	3.498e-04	4.071e+02	9.163e+00	1
201774883	11163452+0454529	169.143833	4.914697	83.505	5.950	1.197e+03	6.494e+02	3.223e+02	2.548e+01	1.453e-02	1.803e-03	3.983e+02	2.150e+01	4.235e-03	3.786e-04	6.295e+02	1.350e+01	1
201781960	11103146+0502268	167.631062	5.040825	81.685	6.281	9.842	0.731	1.279e+03	8.797e+02	4.916e+02	3.903e+01	1.427e-02	1.407e-03	4.465e+02	2.663e+01	4.407e-03	3.542e-04	1.852e+01	1.852e+01	1
201786083	11125055+0506500	168.210683	5.113931	80.724	5.662	5.613	0.018	1.103e+03	6.570e+02	3.848e+02	2.605e+01	1.420e-02	1.407e-03	4.465e+02	2.663e+01	4.407e-03	3.542e-04	7.038e+02	1.520e+01	1
201788284	11101971+0509085	167.582175	5.152367	90.274	4.934	9.987e+02	4.206e+02	2.776e+02	2.451e+01	1.322e-02	1.486e-03	3.942e+02	2.029e+01	3.674e-03	2.790e-04	5.087e+02	4.786e+00	1
201797512	11235883+0519178	170.995146	5.321614	113.952	0.674	7.773e+02	7.031e+01	3.354e+02	1.110e+01	2.149e-02	6.951e-04	2.692e+02	1.141e+01	3.120e-03	1.892e-04	4.833e+02	1.841e+00	2
201797810	11110894+0519882	167.787300	5.327325	82.795	4.936	8.705	0.027	1.988e+03	8.873e+02	3.949e+02	3.293e+01	1.766e-02	2.020e-03	5.200e+02	3.276e+01	3.878e-03	3.651e-04	9.451e+02	2.400e+01	1
201825690	...	167.827858	5.836272	61.013	2.837	3.625e+03	1.530e+03	5.475e+02	3.983e+01	2.117e-02	2.681e-03	6.541e+02	4.011e+01	5.117e-03	4.068e-04	1.739e+03	4.163e+01	1
201830769	11134232+0555598	168.426371	5.933281	83.880	4.531	6.318														

Table 3 (continued)

EPIC	2MASS	RA	Dec	ν_{\max}	$\sigma_{\nu_{\max}}$	$\Delta\nu$	$\sigma_{\Delta\nu}$	A_{\max}	$\sigma_{A_{\max}}$	σ_{meso}	$\sigma_{\tau_{\text{meso}}}$	τ_{meso}	$\sigma_{\tau_{\text{meso}}}$	σ_{gran}	$\sigma_{\tau_{\text{gran}}}$	τ_{gran}	$\sigma_{\tau_{\text{gran}}}$	WN	σ_{WN}	giant? ^a	
		deg	deg	μHz	μHz	μHz	μHz	ppm^2	μHz^{-1}	ppm	μHz^{-1}	μHz^{-1}	ppm	ppm	μHz^{-1}	μHz^{-1}	ppm	ppm^2	μHz^{-1}	ppm^2	μHz^{-1}
201852681	11423531+0621280	175.647167	6.357800	34.347	0.918	3.053	0.016	6.068e+03	1.227e+03	6.915e+02	4.496e+01	3.609e-02	2.687e-03	7.504e+02	2.751e+01	8.389e-03	2.798e-04	9.884e+01	2.325e+00	2	
201877455	11554329+0651459	178.930404	6.862772	83.084	1.515	7.465	0.041	9.033e+02	1.019e+02	6.456e+02	2.115e+01	1.486e-02	8.137e-04	4.026e+02	2.368e+01	4.202e-03	2.230e-04	4.734e+01	1.724e+00	2	
201881721	11505049+0656500	177.710400	6.947208	56.167	3.041	4.883	0.053	2.408e+03	1.224e+03	4.115e+02	2.739e+01	2.580e-02	2.923e-03	5.347e+02	2.637e+01	4.729e-03	2.945e-04	9.605e+02	2.122e+01	1	
201887247	11552041+0703364	178.835058	7.060106	93.323	5.441	8.127e+02	3.055e+02	3.199e+02	1.927e+01	1.462e-02	1.235e-03	3.370e+02	1.832e+01	3.863e-03	3.019e-04	3.730e+02	9.010e+00	1	
201907942	11252290+0729247	171.345400	7.490258	62.643	3.740	9.109	1.316	2.919e+03	1.089e+03	4.923e+02	3.618e+01	2.036e-02	2.139e-03	4.964e+02	3.419e+01	5.737e-03	4.723e-04	1.382e+03	2.843e+01	1	
201908986	11433272+0730459	175.886379	7.512714	92.651	2.459	5.856	0.578	8.239e+02	3.185e+02	3.036e+02	2.007e+01	1.413e-02	1.444e-03	3.869e+02	1.698e+01	3.735e-03	2.881e-04	3.751e+02	1.027e+01	1	
201913188	11515330+0736060	177.972125	7.601786	91.410	3.206	7.372	0.009	1.128e+03	2.642e+02	2.886e+02	2.170e+01	1.397e-02	1.732e-03	4.050e+02	1.973e+01	4.000e-03	2.965e-04	4.892e+02	1.142e+01	1	
201944519	11360006+0818157	174.000267	8.304389	84.794	5.014	1.827e+03	8.741e+02	4.207e+02	3.387e+01	1.372e-02	1.680e-03	6.126e+02	2.536e+01	4.357e-03	3.054e-04	8.930e+02	2.046e+01	1	

^a Certain giants (2) and giant candidates (1). See text for details on the classification.

NOTE—Properties of the C1 solar-like oscillator sample returned by running all non-GAP C1 stars through BAM, and which visual inspection indicated were certain giants ('yes' in the text) or giant candidates ('maybe' in the text). Stars with $\nu_{\max} \lesssim 4\mu\text{Hz}$ should be considered upper limits, as mentioned in the text, and are not assigned errors.

Guest Observer ID	Giant fraction (yes)	Giant fraction (maybe)	Notes
GO1001	0/3	0/3	
GO1002	1/30	0/30	
GO1003	0/2	0/2	Targeted extremely red stars, many likely to be AGB and long-period variables, which would not have been selected by BAM because their frequencies would be below our cutoff of $3\mu\text{Hz}$.
GO1005	0/16	0/16	
GO1006	0/20	0/20	
GO1014	0/1	0/1	
GO1021	0/1	0/1	
GO1023	0/4	0/4	
GO1026	0/2	0/2	Targeted eclipsing binaries, some of which may be giants.
GO1027	2/50	1/50	Targeted AF-type stars, the coolest of which might be oscillating giants.
GO1029	0/1	0/1	
GO1030	0/1	0/1	
GO1036	0/38	0/38	
GO1038	0/12	1/12	Targeted potential oscillators.
GO1040	5/6	0/6	Targeted bright giants.
GO1043	0/25	0/25	
GO1046	0/3	0/3	Targeted bright stars, among them three subgiants, which likely will not oscillate below the long cadence Nyquist frequency of $\sim 283\mu\text{Hz}$.
GO1052	0/1	0/1	
GO1053	0/1	0/1	
GO1054	9/2092	5/2092	
GO1055	0/39	0/39	
GO1057	0/1	0/1	Targeted giant oscillators, and this object was missed by BAM.
GO1061	2/7	0/7	
GO1062	3/4	0/4	
GO1066	3/3	0/3	Targeted subgiants.
GO1068	0/3	0/3	Targeted eclipsing binaries, some of which may be giants.
GO1069	0/6	0/6	
GO1072	0/4	0/4	
GO1073	0/10	0/10	
GO1074	1/3	0/3	Targeted extra-galactic objects.

Table 4. The number of confirmed and marginal giants discussed in this paper found in the observed targets of various Guest Observer proposals gives an indication of the success at rejecting giants using color and proper motion cuts. Note that the tabulated numbers only include targets that had long cadence data. Unless otherwise noted above, the Guest Observer proposals did not, to our knowledge, target giants. We have not listed GO1059, because that is the GAP.

REFERENCES

- Aigrain, S., Parviainen, H., & Pope, B. J. S. 2016, *MNRAS*, 459, 2408
- Anderson, E. R., Duvall, Jr., T. L., & Jefferies, S. M. 1990, *ApJ*, 364, 699
- Angus, R., Foreman-Mackey, D., & Johnson, J. A. 2016, *ApJ*, 818, 109
- Appourchaux, T. 2003, *A&A*, 412, 903
- Armstrong, D. J., Kirk, J., Lam, K. W. F., et al. 2015, *A&A*, 579, A19
- Baglin, A., Michel, E., Auvergne, M., & COROT Team. 2006, in *ESA Special Publication*, Vol. 624, *Proceedings of SOHO 18/GONG 2006/HELAS I, Beyond the spherical Sun*, 34.1
- Bedding, T. R., & Kjeldsen, H. 2010, *Communications in Asteroseismology*, 161, 3
- Bedding, T. R., Huber, D., Stello, D., et al. 2010, *ApJL*, 713, L176
- Borucki, W., Koch, D., Basri, G., et al. 2008, in *IAU Symposium*, Vol. 249, *Exoplanets: Detection, Formation and Dynamics*, ed. Y.-S. Sun, S. Ferraz-Mello, & J.-L. Zhou, 17–24
- Brown, T. M., Gilliland, R. L., Noyes, R. W., & Ramsey, L. W. 1991, *ApJ*, 368, 599
- Chaplin, W. J., Kjeldsen, H., Bedding, T. R., et al. 2011, *ApJ*, 732, 54
- Chib, S., & Jeliazkov, I. 2001, *Journal of the American Statistical Association*, 96, 270.
<https://doi.org/10.1198/016214501750332848>
- Choi, J., Dotter, A., Conroy, C., et al. 2016, *ApJ*, 823, 102
- De Ridder, J., Barban, C., Baudin, F., et al. 2009, *Nature*, 459, 398
- Dotter, A. 2016, *ApJS*, 222, 8
- Foreman-Mackey, D., Hogg, D. W., Lang, D., & Goodman, J. 2013, *PASP*, 125, 306
- Green, P. J. 1995, *Biometrika*, 82, 711.
<https://dx.doi.org/10.1093/biomet/82.4.711>
- Hekker, S., Kallinger, T., Baudin, F., et al. 2009, *A&A*, 506, 465
- Hekker, S., Broomhall, A.-M., Chaplin, W. J., et al. 2010, *MNRAS*, 402, 2049
- Huber, D., Stello, D., Bedding, T. R., et al. 2009, *Communications in Asteroseismology*, 160, 74
- Huber, D., Bedding, T. R., Stello, D., et al. 2010, *ApJ*, 723, 1607
- Huber, D., Bryson, S. T., Haas, M. R., et al. 2016, *ApJS*, 224, 2
- Jeffreys, H. 1935, *Proceedings of the Cambridge Philosophy Society*, 31, 203
- Kallinger, T., Hekker, S., Garcia, R. A., Huber, D., & Matthews, J. M. 2016, *Science Advances*, 2, 1500654
- Kallinger, T., Mosser, B., Hekker, S., et al. 2010, *A&A*, 522, A1
- Kallinger, T., De Ridder, J., Hekker, S., et al. 2014, *A&A*, 570, A41
- Kass, R. E., R. A. E. 1995, *Journal of the American Statistical Association*, 90, 773
- Kjeldsen, H., & Bedding, T. R. 1995, *A&A*, 293, 87
- . 2011, *A&A*, 529, L8
- Luger, R., Agol, E., Kruse, E., et al. 2016, *AJ*, 152, 100
- Lund, M. N., Handberg, R., Davies, G. R., Chaplin, W. J., & Jones, C. D. 2015, *ApJ*, 806, 30
- Mathur, S., García, R. A., Régulo, C., et al. 2010, *A&A*, 511, A46
- Mosser, B., & Appourchaux, T. 2009, *A&A*, 508, 877
- Mosser, B., Belkacem, K., Goupil, M.-J., et al. 2010, *A&A*, 517, A22
- Murphy, S. J., Shibahashi, H., & Kurtz, D. W. 2013, *MNRAS*, 430, 2986
- Nordlund, Å., Stein, R. F., & Asplund, M. 2009, *Living Reviews in Solar Physics*, 6, 2.
<https://doi.org/10.12942/lrsp-2009-2>
- Pinsonneault, M. H., Elsworth, Y. P., Tayar, J., et al. 2018, *ApJS*, 239, 32
- Ricker, G. R., Winn, J. N., Vanderspek, R., et al. 2014, in *Proc. SPIE*, Vol. 9143, *Space Telescopes and Instrumentation 2014: Optical, Infrared, and Millimeter Wave*, 914320
- Scargle, J. D. 1982, *ApJ*, 263, 835
- Schwarz, G. 1978, *Annals of Statistics*, 6, 461
- Sharma, S., Bland-Hawthorn, J., Johnston, K. V., & Binney, J. 2011, *ApJ*, 730, 3
- Sharma, S., Stello, D., Bland-Hawthorn, J., et al. 2019, *arXiv e-prints*
- Skilling, J. 2004, *AIP Conference Proceedings*, 735, 395.
<https://aip.scitation.org/doi/abs/10.1063/1.1835238>
- Stello, D., Cantiello, M., Fuller, J., Garcia, R. A., & Huber, D. 2016, *PASA*, 33, e011
- Stello, D., Chaplin, W. J., Basu, S., Elsworth, Y., & Bedding, T. R. 2009, *MNRAS*, 400, L80
- Stello, D., Huber, D., Kallinger, T., et al. 2011, *ApJL*, 737, L10
- Stello, D., Huber, D., Bedding, T. R., et al. 2013, *ApJL*, 765, L41
- Stello, D., Compton, D. L., Bedding, T. R., et al. 2014, *ApJL*, 788, L10
- Stello, D., Huber, D., Sharma, S., et al. 2015, *ApJL*, 809, L3
- Stello, D., Zinn, J., Elsworth, Y., et al. 2017, *ApJ*, 835, 83

- Ulrich, R. K. 1986, *ApJL*, 306, L37
- Vanderburg, A., & Johnson, J. A. 2014, *PASP*, 126, 948
- Vanderplas, J., Connolly, A., Ivezić, Ž., & Gray, A. 2012, in *Conference on Intelligent Data Understanding (CIDU)*, 47–54
- Watanabe, S. 2013, *Journal of Machine Learning Research*, 14, 867
- Woodard, M. F. 1984, PhD thesis, University of California, San Diego
- Yu, J., Huber, D., Bedding, T. R., et al. 2018, *ApJS*, 236, 42